Available online at www.sciencedirect.com

ScienceDirect

Geochimica et Cosmochimica Acta 238 (2018) 252–269

Geochimica et Cosmochimica Acta

www.elsevier.com/locate/gca

Natural occurrence of nanocrystalline Al-hydroxysulfates: Insights on formation, Al solubility control and As retention

Christoph Wanner [a,*], Rosemarie Pöthig [b], Sergio Carrero [c,d], Alejandro Fernandez-Martinez [e], Christian Jäger [f], Gerhard Furrer [g]

[a] Rock-Water Interaction Group, Institute of Geological Sciences, University of Bern, Baltzerstrasse 3, CH-3012 Bern, Switzerland
[b] Leibniz-Institute of Freshwater Ecology and Inland Fisheries, Berlin, Germany
[c] Department of Earth and Planetary Science, University of California Berkeley, Berkeley, USA
[d] Department of Earth Science, University of Huelva, 21071 Huelva, Spain
[e] Univ. Grenoble Alpes, Univ. Savoie Mont Blanc, CNRS, IRD, IFSTTAR, ISTerre, Grenoble, France
[f] BAM-Federal Institute for Materials Research and Testing, Division I.3, Working Group NMR Spectroscopy, 12489 Berlin, Germany
[g] Institute of Biogeochemistry and Pollutant Dynamics (IBP), Department of Environmental Systems Science, ETH Zurich, 8092 Zurich, Switzerland

Received 30 January 2018; accepted in revised form 23 June 2018; Available online 5 July 2018

Abstract

Nanocrystalline basaluminite $[Al_4OH_{10}(SO_4)\cdot(H_2O)_{3-5}]$ and aggregation of the ε-Keggin polyoxocation $[Al_{12}(AlO_4)(OH)_{24}(H_2O)_{12}]^{7+}$, referred to as Al_{13}, have both been described to form in acid mine drainage environments. Although the chemical composition is quite similar, their crystalline varieties significantly differ, demonstrating that various types of Al-hydroxysulfates can form under similar conditions and that their respective formation is not fully understood yet. Here, we report the occurrence of nanocrystalline precipitates that form naturally in a small alpine catchment in Switzerland where an acidic mountainous stream (pH ~ 4) is neutralized successively after mixing with several neutral tributaries. The stepwise neutralization in conjunction with the large amount of precipitates provide an ideal setting for obtaining new insights into (i) the structure of naturally forming Al-hydroxysulfates, (ii) their formation mechanism, (iii) their role in controlling the solubility of Al, and (iv) their ability to lower the mobility of As. Synchrotron-based high-energy X-ray diffraction and subsequent pair distribution function analyses demonstrate that these precipitates are structurally identical to basaluminite samples obtained from acid mine drainage sites. In contrast, only minor amounts of tetrahedrally coordinated Al, as present in Al_{13}, were identified by nuclear magnetic resonance spectroscopy. The precipitates are further characterized by elevated As concentrations up to 600 μg/g, whereas other heavy metals are at background concentrations only. Given the low As concentrations in the stream from which precipitation occurs (<0.03 mg/L), high As concentrations confirm that basaluminite serves as a highly efficient As sink, which is attributed to its high anion-exchange capacity. Chemical analysis of streamwater samples in combination with geochemical modeling show that precipitation occurs instantaneously upon mixing with neutral streams. Moreover, our data reveal that the precipitation of basaluminite exerts a strong solubility control on dissolved Al concentrations as manifested by the quasi-constant basaluminite ion activity product observed during neutralization from pH 5 to pH 5.9. We hypothesize that in our field system, high fluoride and sulfate concentrations on the order of 100 and 1–2 mg/L,

* Corresponding author.
E-mail addresses: wanner@geo.unibe.ch (C. Wanner), r.poethig@gmx.net (R. Pöthig), sergio.carrero@berkeley.edu (S. Carrero), Alex.Fernandez-Martinez@univ-grenoble-alpes.fr (A. Fernandez-Martinez), christian.jaeger@bam.de (C. Jäger), gerhard.furrer@env.ethz.ch (G. Furrer).

https://doi.org/10.1016/j.gca.2018.06.031

respectively, as well as low water temperatures (<8 °C) favor the formation of basaluminite instead of Al_{13}-bearing sulfate precipitates.

Keywords: Basaluminite; Al_{13}; Acid rock drainage; Arsenic retention; Aluminum; Anion exchange

1. INTRODUCTION

Aqueous Al concentrations are controlled by the pH-dependent solubility of primary alumosilicates as well as the formation of secondary Al-hydroxide phases occurring above pH ~ 4 (Bigham and Nordstrom, 2000). In most acidic systems, gibbsite and kaolinite are the most stable secondary Al phases. However, at elevated aqueous SO_4^{2-} concentrations, such as in the case of acid mine drainage (AMD) and acid sulfate soils (ASS), Al-hydroxysulfates are precipitated instead. Owing to their nanocrystalline occurrence and hence poor crystallinity, the proper characterization of these Al-hydroxysulfates as well as the characterization of precipitates from sites with different conditions is challenging. In the last years, Al-hydroxysulfate precipitates forming in AMD and ASS have been mainly described as basaluminite $[Al_4OH_{10}(SO_4)\cdot(H_2O)_{3-5}]$ (Adams and Rawajfih, 1977; Nordstrom et al., 1984; Ball and Nordstrom, 1989; Bigham and Nordstrom, 2000; Jones et al., 2011; Sánchez-España et al., 2011; Carrero et al., 2015), but other typical examples include aluminite, zaherite, jurbanite and alunite (Bigham and Nordstrom, 2000; Lee et al., 2002; Jones et al., 2011).

Originally, basaluminite was described as a new mineral phase occurring in sedimentary formations with a well-defined crystalline structure (Bannister and Hollingworth, 1948). This is inconsistent with nanocrystalline precipitates observed in many different locations affected by acid water. Farkas and Pertlik (1997) suggested that basaluminite actually represents a microcrystalline variety of the mineral felsöbányaite $[Al_4OH_{10}(SO_4)\cdot 5H_2O]$. This led the International Mineralogical Association (IMA) to discredit basaluminite as a mineral. Carrero et al. (2017a) suggested that the ambiguity about the nature of basaluminite arises from the difficulty to characterize such nanocrystalline structures. They combined high-energy X-ray diffraction spectroscopy and reverse Monte Carlo modeling, which confirmed the close structural similarity between basaluminite and felsöbányaite. In addition, Carrero et al. (2017a) suspected that the structural and chemical similarities between these two phases could be fortuitous due to the lack of correlation between spatial occurrence and formation conditions.

In addition to basaluminite, the precipitation of nanocrystalline Al-hydroxysulfates has been described to include the ε-Keggin polyoxocation $[Al_{12}(AlO_4)(OH)_{24}(H_2O)_{12}]^{7+}$, commonly referred to as Al_{13} (Ulrich and Pöthig, 2000; Furrer et al., 2002; Kim, 2015). These authors report that the precipitates may contain significant amounts of tetrahedrally coordinated Al (Al[4]) that are close to 7.6%, the stoichiometric fraction in Al_{13}. Similarly, Al-hydroxysulfate precipitates resulting from titration of lake waters originating from AMD and from titration of aqueous ASS or AMD solutions have been described as basaluminite (Sánchez-España et al., 2011; Carrero et al., 2015), or as aggregation of various Al-hydroxysulfates including Al_{13}-bearing sulfates (Totsche et al., 2003). Although the chemical composition and formation condition of Al_{13}-bearing sulfates and basaluminite are quite similar, Al_{13}-bearing sulfate crystals (Johansson, 1960, 1963) are structurally distinct from felsöbányaite (Farkas and Pertlik, 1997) (see structural models provided in Fig. S1, Electronic Annex). This is relevant because the latter has a chemical and crystal structure that is very similar to that of basaluminite (Carrero et al., 2017a). Thus, various types of nanocrystalline Al hydroxysulfates can form under similar conditions and their respective formation is not fully understood yet. Nanocrystalline Al-hydroxysulfates have the potential to control the mobility of major (Al and S) and trace elements (e.g., As and Se) and hence to affect the quality of surface waters (Munk et al., 2002; Sánchez-España et al., 2006; Liu and Zhao, 2009; Mertens et al., 2012; Carrero et al., 2017b).

In this work, we report the occurrence of nanocrystalline Al-hydroxysulfates naturally precipitated over several hundred meters along a stream in a small alpine catchment in Switzerland. The stepwise neutralization of an acidic stream by mixing with several circumneutral streams along the flow provides an ideal setting for obtaining new fundamental insights into (i) the structure of naturally forming Al-hydroxysulfates, (ii) their formation mechanism, (iii) their role in controlling the solubility of Al, and (iv) their ability to lower the mobility of As. To elucidate these points, we present data from a large number of chemical water analyses, synchrotron-based high-energy X-ray diffraction analysis, nuclear magnetic resonance and infrared spectroscopy, and results from geochemical modeling.

2. SITE DESCRIPTION

The study area encompasses a remote area with no mining and very little other anthropogenic (i.e., agricultural) activity at an altitude of 2300–2800 m a.s.l. located in the Engadin area, Switzerland, close to the Swiss-Italian boarder (Fig. 1). Geologically, it is part of the Languard nappe, which belongs to the crystalline basement of the upper Austroalpine unit of the Alps, mainly exposed in Eastern Switzerland and Austria (Schmid et al., 2004). Two main rock types are exposed in the study area, (i) a chlorite mica-schist of sedimentary origin, and (ii) a coarse-grained, leucocratic metagranite (Peters, 2005). In addition, quaternary weathering products of these units such as moraines and alluvial cones cover a substantial part of the study area.

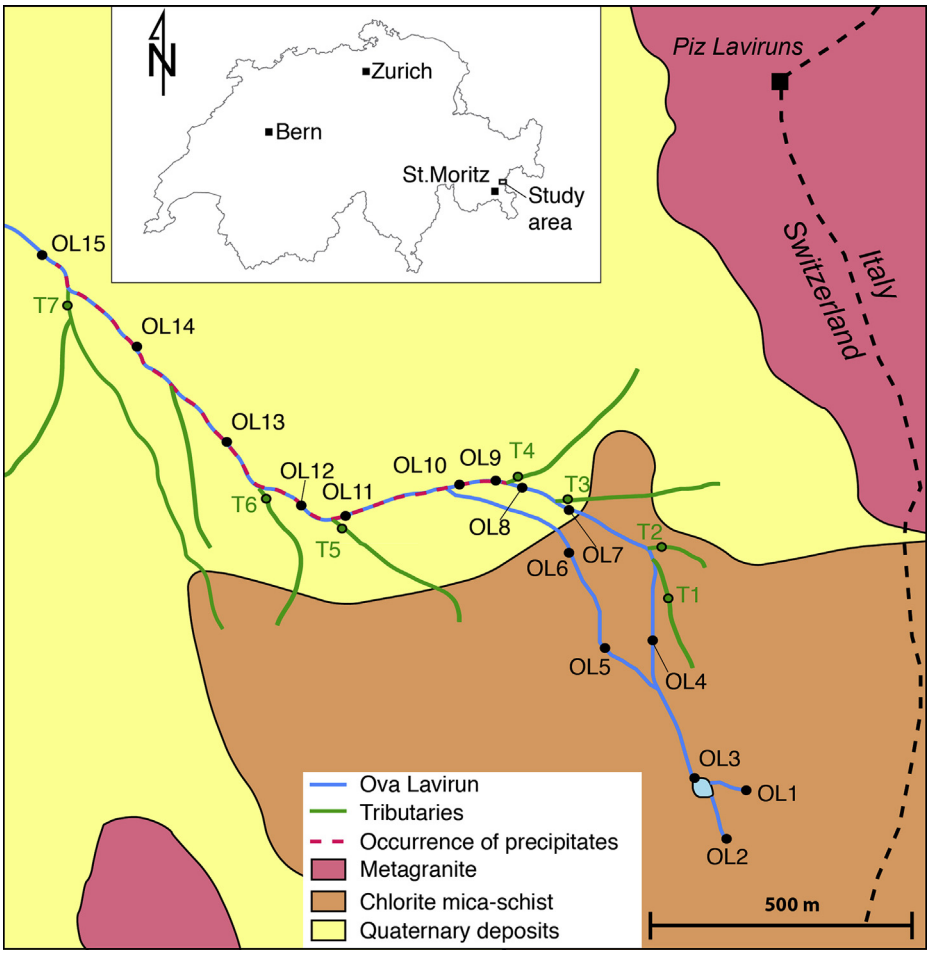

Fig. 1. Geological map (modified from Swisstopo, 2017) of the study area showing the courses of the slightly acidic Ova Lavirun stream and its circumneutral tributaries. Black (OL1–OL15) and green (T1–T7) symbols show the corresponding sampling points. The red dashed line (from OL9 to OL15) indicates the stream segment along which Al-hydroxysulfate precipitation was observed. (For interpretation of the references to colour in this figure legend, the reader is referred to the web version of this article.)

The precipitation of Al-hydroxysulfates is manifested by white coatings on the bedload of the small mountainous stream "Ova Lavirun" (Fig. S2, Electronic Annex). The coatings are observed over a flow distance of about 1.1 km, whereas the thickness gradually decreases from ~2 mm to just a couple of microns. Ova Lavirun originates ca. 600 m upstream of the first occurrence of the precipitates at the outlet of a small water pond with a surface area of about 100–200 m^2 (Fig. S3, Electronic Annex). The pond is characterized by a slightly acidic pH of about 4.5 and an elevated total dissolved solid (TDS) concentration of >1000 mg/L. The low pH observed in Ova Lavirun is due to the oxidation of pyrite occurring naturally in the finer-grained portion of the chlorite mica-schist bedrock. This rock is exposed at the origin of Ova Lavirun (Fig. 1) and shows a typical rusty patina from oxidative pyrite weathering (Fig. S4, Electronic Annex). Upstream of the pond, kinetically controlled pyrite oxidation (Williamson and Rimstidt, 1994) and hence acid generation (Evangelou and Zhang, 1995 and references therein) is facilitated by the occurrence of slow subsurface flow, which is manifested by (i) the imbalance between superficial in- and outlets at the acidic pond, (ii) the relatively low slope in the vicinity of the pond (<10°), and (iii) the occurrence of unconsolidated sediments (e.g., blocks and rocks from rockfall). Along its flow path, Ova Lavirun is continuously diluted and neutralized by merging with several circumneutral tributaries characterized by low TDS concentrations (Fig. 1). About 200 m downstream of the acidic pond, the stream Ova Lavirun is forked into two fractions, which meet again downstream of the occurrence of the first precipitates.

Due to the high altitude, the study area is typically covered by snow from November to June. Discharge rates of Ova Lavirun and its tributaries are at their maxima during snowmelt in June (≥0.1 m^3/s). In the subsequent months, discharge rates are strongly variable in response to the course of atmospheric precipitation and temperature variation.

3. METHODS

3.1. Sampling

A total of 29 streamwater samples from 22 locations (Fig. 1) were collected during two sampling campaigns in 2015 (September 21–22), and 2016 (July 1–2). According to runoff records in La La Punt Chamues-ch, approximately 10 km downstream from the study area, the September 2015 campaign was carried out when the discharge was close to the annual average (about 2.3 m^3/s), whereas the July 2016 campaign was during the peak of snowmelt when the discharge was slightly more than three-fold above average (7.5 m^3/s) (FOEN, 2016). Leftover snow cover was the reason why samples OL1–OL3 (i.e., acidic pond and its inlets) could not be collected in July 2016. The pH value, dissolved O_2, electrical conductivity, and sampling temperature were measured on-site using Hamilton industrial electrodes with Knick Portamess-913 field instruments. After collection, three aliquots per sample were filtered at 0.45 μm and stored in polyethylene bottles. The aliquots for the analysis of major ions and heavy metals were acidified with 1 mL of 65% HNO_3. After transporting to the laboratory, samples were stored at 4 °C. During the July 2016 sampling campaign, one aliquot per sample was additionally cooled using a cool box, avoiding significant temperature changes between sampling at 2–8 °C and determining aqueous Al speciation by the Ferron method as described below.

White precipitate samples from Ova Lavirun were obtained by scratching from air-dried rock specimen collected along the Ova Lavirun streambed using a stainless steel spatula. It should be noted that the collected precipitates formed over a certain amount of time and hence do not fully correspond to the collected streamwater samples, representing one particular point in time. Moreover, we cannot fully exclude structural changes due to dehydration occurring between sampling in the field and actual analyses.

The precipitates from Ova Lavirun were compared to natural and synthetic basaluminite extensively characterized by Carrero et al. (2017a), as well as synthetic Al_{13} sulfate. In that study, what Carrero et al. (2017a) called natural basaluminite was precipitated by slow titration under continuous stirring of an AMD solution from the Tinto river (Iberian Pyrite Belt, SW Spain) using a 0.01 mol/L $Ca(OH)_2$ solution, as described by Carrero et al. (2015). Because the expression natural basaluminite is not fully appropriate, this sample will be referred to as AMD-titrated basaluminite throughout this paper. Synthetic basaluminite was prepared by drop-by-drop addition of 214 mL of a 0.015 mol/L $Ca(OH)_2$ solution to 30 mL of 0.05 mol/L $Al(SO_4)_3{\cdot}18H_2O$ under continuous stirring, according to the method described by Prietzel and Hirsch (1998). Each solid sample was washed several times with deionized water to dissolve possible co-precipitated mineral phases. Synthetic Al_{13} sulfate was precipitated with excess Na_2SO_4 from an $AlCl_3$ solution with Al/Si and OH/Al ratios of 12 and 2.4, respectively, and containing about 70% Al_{13} (Fig. S5, Electronic Annex).

3.2. Analytical methods

3.2.1. Streamwater analyses

Concentrations of major cations (Na^+, K^+, Ca^{2+}, Mg^{2+}) and anions (F^-, Cl^-, NO_3^-, SO_4^{2-}) of streamwater samples were determined at the University of Bern by ion chromatography (IC) using a Metrohm 850 system. The detection limit was 0.016 mg/L for anions and 0.1 mg/L for cations and the analytical error was ±5% based on multiple measurements of high-grade standard solutions (Sigma-Aldrich, Merck). Total inorganic carbon concentrations were determined using a TIC/TOC analyzer (Analytic Jena multi N/C 2100S) with a detection limit of 0.1 mg/L and an analytical uncertainty of ±5%. The aqueous concentrations of As, Al, Ba, Cu, Fe, Mn, Ni, Zn, Si, Sr, Pb and Cd were determined by inductively coupled plasma optical emission spectroscopy (ICP-OES) using a Varian 720-ES ICP spectrometer at the University of Bern with detection limits of 1 μg/L for Mn, Ba, Sr and Zn, 3 μg/L for Al and Si, 5 μg/L for Fe, Ni, Cd and Cu, 10 μg/L for As, and 20 μg/L for Pb. The analytical uncertainty is element specific and within the range of ±5–10% depending on element concentration and sample matrix, and based on multiple measurements of high-grade standard solutions (Sigma-Aldrich, Merck).

The mononuclear and polynuclear Al species distribution in streamwater samples were determined at the Leibniz-Institute of Freshwater Ecology and Inland Fisheries, Berlin using the Ferron method as described by Schönherr et al. (1983, 1987) and Bertram et al. (1994). This photometric/kinetic method makes use of the fact that mononuclear Al species react instantaneously with an acetate-buffered ferron solution (8-hydroxy-7-iodchino line-5-sulfonic acid) at pH 5. In contrast, polynuclear Al species react by pseudo-first-order kinetics to disintegrate into mononuclear Al species before the detectable Al-ferron complex can be formed. For this study, Al calibration solutions were obtained by dilution of a Merck standard solution (1 g/L Al) into the concentration range of the water samples (0.5–50 mg/L Al). For analysis one mL per water sample was quickly added to 9 mL buffer and 3 mL Ferron solutions prior to starting the measurement (accuracy ±2%) in 1 cm cuvettes at $\lambda = 368$ nm within 30 s using a UV–Vis-scanning spectrophotometer from Shimadzu (UV-2401PC). The kinetic curves obtained from the Ferron method were analyzed according to the method of Schönherr et al. (1983, 1987) modified by computer-aided calculation. To do so, the absorbance data of the time curves were converted into the logarithm of non-reacted Al. Subsequently, the concentrations of monomeric Al, and polymeric species different than Al_{13} (Al_x) were determined from the intersections of the tangents at $t = 0$ of the initial (Al_{mono}) and second linear part (Al_x) of the converted time curves, respectively (Fig. S6, Electronic Annex). The concentration of Al_{13} was calculated from the difference between 100 and the sum of the concentrations of Al_x and Al_{mono}. The actual type of the existent Al species in the samples was determined from the rate constants, which was calculated from the gradients of the two linear parts of the converted time curves. Such identification is based on

the comparison with ^{27}Al NMR data from which it is known that the first linear part of the time curves with a rate constant of about 0.12 min^{-1} is equitable to Al_{13} (Schönherr et al., 1983; Parker and Bertsch, 1992). The second linear part with a rate constant of 0.002 min^{-1} described as Al_{poly} in Schönherr et al. (1983, 1987) and Bertram et al. (1994) correspond to the Al_{30} polycation first described in the year 2000 (Allouche et al., 2000; Rowsell and Nazar, 2000). Moreover, it is known that transitional polymers (Al_{tp}) with rate constants between those of Al_{13} and Al_{30} exist in addition to Al_{13} and Al_{30} (Bertram et al., 1994). The fractions of aqueous Al species determined via Ferron kinetics or ^{27}Al NMR spectroscopy has been assessed to be equivalent (Changui et al., 1990; Parker and Bertsch, 1992; Bertram et al., 1996).

3.2.2. Analyses of white precipitates

Elemental analysis of the precipitates was performed at the University of Bern by digestion of 0.05 g of samples in 5 mL of 65% HNO_3, following the protocol described by Carrero et al. (2017b). Subsequently, concentrations of Al, S, Si, As, K, Na, Fe and Ca were determined by ICP-OES. Sulfur concentrations were converted to SO_4 as inferred from the high SO_4 concentrations and oxidizing conditions in the stream (Table 1). The combined H_2O and OH content was derived from the difference between the sum of the weight percent obtained for the elements analyzed by ICP-OES and 100%, which was within ±3 wt% of the weight loss measured when exposing the samples to 1050 °C during 2 h (i.e., loss on ignition).

The structure of the precipitates was investigated by synchrotron-based high-energy X-ray diffraction (HEXD) in combination with subsequent pair distribution function (PDF) analysis, as well as infrared (IR) and ^{27}Al magic-angle sample spinning nuclear magnetic resonance (^{27}Al MAS NMR) spectroscopy. HEXD and PDF were performed at beamline ID31 at the European Synchrotron Radiation Facility (ESRF) in Grenoble, providing a monochromatic X-ray beam with energy of ~78.3 keV ($\lambda = 0.1583$ Å) in Debye-Scherrer geometry. The energy was calibrated using a CeO_2 standard (NIST 679b). Samples were loaded in polyimide (Kapton) capillaries. The diffraction patterns were collected using a Perkin-Elmer flat-panel detector and were integrated using the software PyFAI (Kieffer and Karkoulis, 2013). PDFs were obtained by Fourier transformation of the structure factor (S(Q); $Q_{max} = 27.0$ $Å^{-1}$), with the background scattering corrected using the software PDFgetX3 (Juhas et al., 2013).

IR spectroscopy was performed at the Leibniz-Institute of Freshwater Ecology and Inland Fisheries in Berlin. Five to six mg of air-dried samples were ground together with 800 mg dried KBr (105 °C) and pressed under vacuum conditions into disks of 20 mm diameter. Infrared spectra were recorded with a Fourier-transform spectrometer (IR-Tracer-100, Shimadzu) over a range of 400–4000 cm^{-1} with 2 cm^{-1} resolution and 100 scans. Since the recorded IR spectra showed a low resolution, the absorption bands were identified by calculating the second derivative. Subsequently, band component analysis was carried out with TOPAS-Academic (Coelho, 2016) using a pseudo Voigt function (i.e., Gauss-Lorentz cross product) with a Gauss-Lorentz ratio greater than 0.8 and a flat background. Wavenumbers of absorption bands were fixed to the values obtained during band identification, whereas relative intensities and peak widths were refined by non-linear least squares for each spectrum. Fitting was undertaken until reproducible results were obtained with a goodness of fit smaller than 0.1.

^{27}Al MAS NMR spectroscopy was carried out at the BAM – Federal Institute of Materials Research and Testing in Berlin, using a Bruker Avance 600 spectrometer with 4 mm rotor system operating at 156.4 MHz, 12.5 kHz MAS, and a selective 90° pulse width p(sel) = 2.5 µs. For each analysis, 128 scans were accumulated. The proportion of four-, five-, and six-fold coordinated Al were estimated by calculating the relative intensity area below the peaks representing the corresponding coordination states, which are at about 64 (Al[4]), 36 (Al[5]), and near zero ppm (Al[6]) chemical shift (Furrer et al., 2002) assuming similar quadrupole interaction for all sites. The recorded spectra were fitted with TOPAS-Academic (Coelho, 2016) using pseudo Voigt peaks and a flat background. Peak asymmetry was modeled using a circular convolution.

3.3. Geochemical modeling

Aqueous speciation calculations were performed with the geochemical modeling software PHREEQC V3 (Parkhurst and Appelo, 2013) using the WATEQ4F database, in which temperature dependent equilibrium constants are tabulated for the monomeric Al species Al^{3+}, $Al(OH)^{2+}$, $Al(OH)_2^+$, $Al(OH)_3$, $Al(OH)_4^-$, AlF^{2+}, AlF_2^+, $AlSO_4^+$, $Al(SO_4)_2^-$, and $AlHSO_4^{2+}$ (Ball and Nordstrom, 1991). To assess the relevance of the polymeric Al_{13} complex in our streamwater samples, the database was enlarged with the ε-Keggin polyoxocation $[Al_{12}(AlO_4)(OH)_{24}(H_2O)_{12}]^{7+}$ by adding the aqueous complexation reaction:

$$13Al^{3+} + 40H_2O = Al_{13}O_4(OH)_{24}(H_2O)_{12}{}^{7+} + 32H^+ \quad (1)$$

Plyasunov and Grenthe (1994) have presented a model for calculating the temperature dependence of the equilibrium constant for this reaction (i.e., log(K) value). Because the sampling temperature of our streamwater samples is within 2–8 °C and the model of Plyasunov and Grenthe (1994) predicts an almost linear dependence between 0 and 25 °C, we applied a linear interpolation to the log(K) values tabulated at 0 and 25 °C (−117.24 and −98.52, respectively) to account for the temperature dependence of the log(K) value of the aqueous Al_{13} complex.

4. RESULTS

4.1. Streamwater samples

4.1.1. General chemical composition

The chemical composition of streamwater samples collected during the two sampling campaigns are listed in Table 1 and in the Electronic Annex (Tables S1 and S2). Concentrations of the major cations and anions are plotted on a classical Piper diagram (Fig. 2). According to the

Table 1
Key parameters of streamwater samples collected (a) during the September 2015, and (b) the 2016 sampling campaigns. Also shown are the logarithmic values of the basaluminite ion activity product (log(*IAP*), and the contribution of Al-F complexes (AlF_2^+, AlF^{2+}) as well as aqueous $AlSO_4^+$ and Al_{13} on total dissolved Al, all calculated using PHREEQC. The full chemical analyses and the PHREEQC in- and output files are provided as Electronic Annexes.

(a) Sept. 2015	OL1	OL2	OL3	OL4	OL6	OL7	OL8	OL9	OL10	OL11	OL13	OL15	T2	T3	T4	T6	T7
Distance from lake (m)	−200	−100	0	300	600	400	700	720	850	1000	1200	1800	n.a.	n.a.	n.a.	n.a.	n.a.
T sampling (°C)	2.0	4.0	6.3	6.5	5.6	8.4	8.3	8.5	6.2	5.8	5.7	4.8	8.5	7.9	8.6	5.4	5.1
pH on-site	4.06	4.5	4.67	4.64	4.73	4.9	5.05	5.45	5.43	5.32	5.9	7.26	6.77	5.7	6.69	6.8	7.28
Al (mg/L)	40.1	5.54	19.7	12.29	8.89	3.92	3.30	1.760	1.749	2.00	0.532	0.048	0.013	0.068	<0.003	<0.003	<0.003
As (mg/L)	<0.01	<0.01	<0.01	<0.01	<0.01	<0.01	<0.01	<0.01	<0.01	<0.01	<0.01	<0.01	<0.01	<0.01	<0.01	<0.01	<0.01
SO_4^{2-} (mg/L)	1738.5	643	1067	746	532	267	234	165	167	181	117	76.8	71.1	62.0	9.20	30.6	31.4
HCO_3^- (mg/L)	0.0	4.9	3.7	4.3	4.3	4.3	4.27	4.3	4.9	4.3	4.88	34.2	6.7	6.1	31.1	16.5	47.6
F^- (mg/L)	12.6	1.45	8.99	3.22	2.26	1.06	0.899	0.681	0.681	0.749	0.463	0.299	0.090	0.086	0.208	0.140	0.168
Water type	Mg-Ca-SO_4	Mg-Ca-SO_4	Mg-Ca-SO_4	Mg-Ca-SO_4	Mg-Ca-SO_4	Mg-Ca-SO_4	Mg-Ca-SO_4	Mg-Ca-SO_4	Mg-Ca-SO_4	Mg-Ca-SO_4	Mg-Ca-SO_4	Mg-Ca-SO_4-HCO_3	Mg-Ca-SO_4	Mg-Ca-SO_4	Ca-(Mg)-HCO_3-SO_4	Ca-Mg-SO_4-HCO_3	Ca-Mg-Na-HCO_3-SO_4
Al/SO_4 (mol ratio)	0.08	0.03	0.07	0.06	0.06	0.05	0.05	0.04	0.04	0.04	0.02	0.00	0.00	0.00	n.a.	n.a.	n.a.
[1]$Log(IAP)_{basaluminite}$	22.93	25.17	27.99	27.82	28.55	29.36	30.68	32.58	32.97	32.40	33.19	33.33	31.18	28.35	n.a.	n.a.	n.a.
[2]$Log(IAP)_{basaluminite}$	20.72	22.71	25.48	25.31	25.97	26.67	27.91	29.61	30.01	29.50	30.01	29.53	27.56	25.19	n.a.	n.a.	n.a.
[3]$AlSO_4^+$	43.62	45.97	33.15	46.51	45.63	39.68	37.85	15.26	21.17	27.29	3.70	0.01	0.19	3.86	n.a	n.a	n.a
[3]$AlF_2^+ + AlF^{2+}$	38.49	33.55	53.03	33.47	32.85	35.15	35.38	45.60	47.53	46.82	75.56	6.27	16.01	81.40	n.a	n.a	n.a
[3]Al_{13} ($T = T_{sampling}$)	0.0	0.0	0.0	0.0	0.0	0.0	0.0	20.2	7.6	0.1	8.4	0.3	0.0	0.0	n.a.	n.a.	n.a.
[3]Al_{13} (T = 25 °C)	0.0	0.0	0.0	0.0	0.8	13.5	37.4	55.2	53.7	48.8	39.4	0.0	0.0	0.0	n.a.	n.a.	n.a.

(b) July 2016	OL4	OL7	OL8	OL9	OL11	OL12	OL13	OL14	OL15	T1	T4	T5
Distance from lake (m)	300	400	700	720	1000	1050	1200	1500	1800	n.a.	n.a.	n.a.
T sampling (°C)	0.9	3.5	4.0	6.1	7.0	7.0	7.6	7.7	7.5	1.0	6.4	3.5
pH on-site	4.49	4.82	4.92	5.29	4.88	5.23	5.24	5.74	6.48	6.41	6.42	6.56
Al (mg/L)	21.88	3.015	2.553	1.599	5.513	4.386	2.888	0.865	0.207	0.016	<0.003	<0.003
As (mg/L)	0.114	0.016	0.015	0.011	0.024	0.022	0.017	0.011	<0.01	<0.01	<0.01	<0.01
SO_4^{2-} (mg/L)	926.7	148.5	134.6	93.8	243.6	220.3	144.0	105.5	82.2	16.2	4.85	26.2
F^- (mg/L)	5.230	0.717	0.632	0.501	1.347	1.177	0.805	0.584	0.418	0.095	0.215	0.095
HCO_3^- (mg/L)	3.6	2.0	1.7	2.5	2.1	2.5	2.5	2.6	6.9	4.3	14.5	9.2
Water type	Mg-Ca-SO_4	Mg-Ca-SO_4	Mg-Ca-SO_4	Mg-Ca-SO_4	Mg-Ca-SO_4	Mg-Ca-SO_4	Mg-Ca-SO_4	Mg-Ca-SO_4	Mg-Ca-SO_4	Mg-Ca-Na-SO_4-(HCO_3)	Ca-Na-HCO_3-SO_4	Ca-Mg-Na-SO_4-HCO_3
Al/SO_4 (mol ratio)	0.08	0.07	0.07	0.06	0.08	0.07	0.07	0.03	0.01	0.04	n.a.	n.a.
[1]$Log(IAP)_{basaluminite}$	27.23	28.74	29.50	32.30	29.94	32.45	32.53	32.79	33.00	30.61	n.a.	n.a.
[2]$Log(IAP)_{basaluminite}$	24.80	26.04	26.75	29.37	27.25	29.63	29.65	29.67	29.55	27.05	n.a.	n.a.
[3]$AlSO_4^+$	48.60	37.25	35.20	24.53	41.04	36.24	28.74	4.50	0.21	0.28	n.a	n.a
[3]$AlF_2^+ + AlF^{2+}$	30.80	31.71	32.92	40.65	32.19	34.96	36.21	64.81	69.69	82.52	n.a	n.a
[3]Al_{13} ($T = T_{sampling}$)	0.0	0.0	0.0	0.1	0.0	0.7	4.9	18.2	13.3	0.0	n.a.	n.a.
[3]Al_{13} (T = 25 °C)	0.0	0.0	1.6	13.9	50.0	26.0	57.7	57.6	44.2	33.8	n.a.	n.a.

[1] Refers to the inferred basaluminite stoichiometry of $Al_4(OH)_{10.43}(SO_4)_{0.79}\cdot 2.2H_2O$.
[2] Refers to the ideal basaluminite stoichiometry of $Al_4OH_{10}(SO_4)\cdot 5H_2O$.
[3] % of Al_{total}.

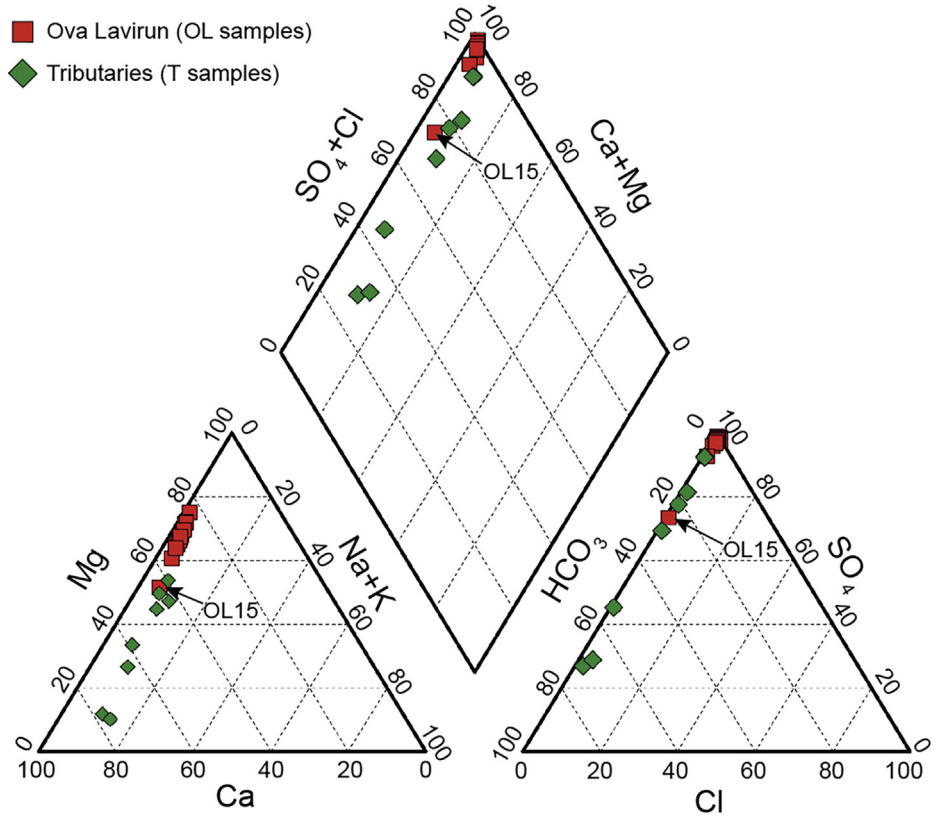

Fig. 2. Piper diagrams for the streamwater samples collected during the two field campaigns in September 2015 and July 2016. Squares denote samples collected along Ova Lavirun (OL samples), whereas diamonds refer to tributaries to Ova Lavirun (T samples). As example, Sample OL15 is indicated by an arrow.

water classification of Jäckli (1970), Ova Lavirun (i.e., OL) samples correspond to a Mg-Ca-SO_4 water type. With the exception of sample OL15, all Ova Lavirun samples are acidic (pH: 4.1–5.9), characterized by high Mg, Ca, Al and SO_4 concentrations, a slightly elevated Ni, Zn and Mn content, and appear on the same region on the Piper diagram subplots (Fig. 2). The lowest pH (4.1) and highest elemental concentrations (e.g., SO_4: 1738 mg/L; Mg: 239 mg/L, Ca: 159 mg/L; Al: 40.1 mg/L) were observed at one of the two superficial inlets to the acidic pond (sample OL1, Fig. 1). While the low pH and elevated SO_4 concentrations result from pyrite oxidation, high Mg, Ca, and Al concentrations are due to the dissolution of alumosilicates such as mica, chlorite, and feldspars, which is promoted by the low pH and consequently supported by increased solubility (Ghebremedhin, 2017). A closely related two-step process (i.e., pyrite oxidation and subsequent dissolution of other minerals) has been addressed to explain elevated SO_4, Ca, and Mg concentrations observed in a similar high alpine catchment in Switzerland (Bucher et al., 2017).

In contrast to Ova Lavirun, its tributaries (i.e., T samples, Fig. 1) show low TDS concentrations (<105 mg/L), circumneutral pH values, and higher concentrations of calcium and bicarbonate, although the water type is variable (Table 1). In each Piper diagram subplots, the T samples plot on straight lines between SO_4^{2-} and Mg-rich, and HCO_3^- and Ca-rich endmembers (Fig. 2), demonstrating that they represent a binary mixture. These endmembers are inherited from the two main lithologies exposed in the study area. Similar to the origin of Ova Lavirun, tributaries T1–T3 are exclusively affected by the pyrite-bearing chlorite mica-schist bedrock (Fig. 1) and show the same general water type (i.e., Mg-Ca-SO_4, Table 1). The pH, however, is higher (pH: 5.7–6.8) than along the upper part of Ova Lavirun (pH < 5) due to the steeper slope limiting the subsurface residence time and hence pyrite oxidation. In contrast, tributaries (T4–T7) are additionally affected by the exposed metagranite unit and/or its quaternary weathering products (Fig. 1). Both are calcite-bearing and pyrite-free, and hence they generate waters of a general Ca-Na-HCO_3 type, corresponding to the second endmember type.

4.1.2. Chemical evolution along Ova Lavirun

Due to the merging tributaries, metal concentrations and pH of Ova Lavirun are continuously diluted and neutralized as illustrated by the TDS and pH evolution along its flow path (Fig. 3a and b). Over the first 800 m a strong TDS decrease by a factor of ~5 is observed when Ova Lavirun merges with tributaries T1–T3, whereas the pH remains below 5 due to the weak neutralizing capacity of these tributaries (i.e., low HCO_3^- concentrations, Mg-Na-SO_4 waters). Merging with tributary T4 then causes a strong pH increase of about 0.4 units and the pH reaches

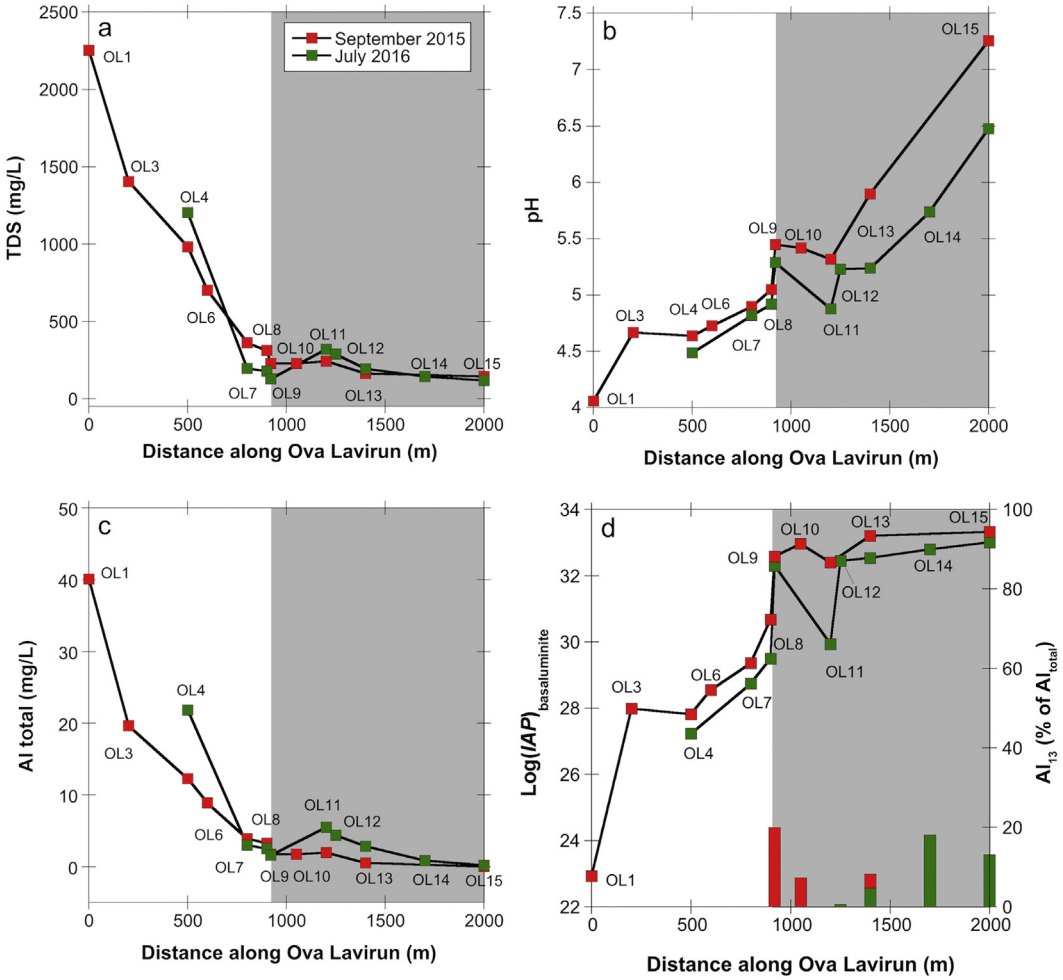

Fig. 3. Evolution of the (a) total dissolved solid concentration (TDS), (b) pH, (c) total Al concentration (precise values are listed in Tables 1 and 2), and (d) logarithm of the basaluminite ion activity product, along the course of Ova Lavirun in September 2015 (red) and July 2016 (green). The logarithm of the basaluminite ion activity product was calculated using PHREEQC for the proposed basaluminite stoichiometry of $Al_4(OH)_{10.43}(SO_4)_{0.79}{\cdot}2.2H_2O$ ($\log(IAP) = 4 \times \log(a_{Al3+}) + 0.79 \times \log(a_{SO4}) + 10.43$ x pH). Bars shown in (d) illustrate the calculated contribution of the aqueous Al_{13} complex on total dissolved Al for the September 2015 and July 2016 sampling campaigns, respectively. Gray domains illustrate the segment along Ova Lavirun where precipitates were visible. (For interpretation of the references to colour in this figure legend, the reader is referred to the web version of this article.)

a value significantly above 5 at location OL9 (Sept. 2015: 5.45; July 2016: 5.29). This pH jump is due to the rather strong neutralizing capacity of T4 manifested by its elevated HCO_3^- concentration of up to 31 mg/L (Table 1), inherited from draining weathering products of the metagranite unit outcropping at the Western flank of the peak Piz Laviruns (Fig. 1). Moreover, the pH jump coincides with the first visible occurrence of Al-hydroxysulfates, confirming that the pH is the main driver for precipitation (Furrer et al., 1992a, 1992b; Totsche et al., 2003; Sánchez-España et al., 2011; Carrero et al., 2015). Depending on the discharge conditions, the pH may drop again below 5 at OL11 upon merging with the Western fork of Ova Lavirun (e.g., July 2016) before being further neutralized by tributaries T5–T7, also showing significant HCO_3^- concentrations (Table 1). At the last occurrence of the precipitates at OL15, the pH has increased to values ≥6.5.

Prior to the first occurrence of the precipitates at OL9, Al concentrations have decreased from ~20 mg/L at the outlet of the acidic pond (at OL3) to about 2.5–3.5 mg/L (Fig. 3c), consistent with the decrease in TDS and major cation and anion concentrations (Tables 1). Subsequently, the Al concentration approaches zero, whereas the TDS concentration only shows a minor decrease, approaching the TDS concentrations of the tributaries (Fig. 3a).

4.1.3. Al speciation

The results of the Ferron method applied to streamwater samples obtained from the two sampling campaigns are shown in Table 2. Most samples showed more than 90% mononuclear Al. However, three samples collected in 2016 along the section with visible precipitates yielded high to very high portions (36–97%) of Al polymers with particularly low and undefined rate constants of 0.011–0.043 min^{-1}.

Table 2
Results from the Ferron method applied to determine the Al speciation of selected Ova Lavirun streamwater samples collected during the September 2015 campaign and of all samples collected in July 2016.

		pH field	$T_{transport}$[1] (°C)	pH lab	Al_{total} (mg/L)	Al_{mono} (%)	Al_{13} (%)	Al_{tp}[2] (%)	k (Al_{13}) (min^{-1})	k (Al_{tp}) (min^{-1})
Sept.2015	OL1	4.06	22	3.90	40.88	95.7	1.2	3.1	0.121	0.0230
	OL3	4.67	22	4.19	20.17	96.2	1.2	2.6	0.118	0.0193
	OL4	4.64	22	4.24	12.81	95.3	0.9	3.8	0.125	0.0253
	OL8	5.05	22	4.74	3.61	92.7	1.9	5.4	0.092	0.0226
July 2016	OL4	4.49	7	4.38	25.7	93.2	3.9	2.9	0.119	0.0143
	OL7	4.82	7	5.07	3.19	87.5	0.0	12.5	n.d.	0.0122
	OL8	4.92	7	5.1	2.59	85.9	0.0	14.1	n.d.	0.0090
	OL9	5.29	7	5.07	1.68	85.7	0.0	14.3	n.d.	0.0175
	OL11	4.88	7	4.77	6.34	92.9	0.0	7.1	n.d.	0.0184
	OL12	5.23	7	4.85	5.15	96.2	1.2	2.6	0.124	0.0190
	OL13	5.24	7	5.09	2.66	64.0	0	36.0	n.d.	0.0111
	OL14	5.74	7	5.11	0.95	31.4	4.5[3]	64.1	0.028[3]	0.0106
	OL15	6.48	7	5.7	0.40	2.6	0	97.4	n.d.	0.0432

n.d.: not detected.
[1] Only the samples collected during the 2016 campaign were cooled during transportation to the laboratory.
[2] Al_{tp} signifies transitional polymers with rate constants between those of Al_{13} (0.12 min^{-1}) and Al_{30} (~0.002 min^{-1}) (Bertram et al., 1994).
[3] A rate constant of 0.028 min^{-1} is not consistent with Al_{13}. Thus, the indicated Al_{13} content refers to an Al polymer of unknown structure.

Since these constants lie between those of Al_{13} (~0.12 min^{-1}) and Al_{30} (~ 0.002 min^{-1}) they are referred to as transitional Al polymers (Al_{tp}) of unknown structure (Bertram et al., 1994). Finally, in any of the samples the percentage of Al_{13} cations with a typical rate constant of about 0.12 min^{-1} was very low (0–3.9%).

4.2. White precipitates

4.2.1. Structural characterization

4.2.1.1. High-energy X-ray diffraction (HEXD). Diffraction patterns and pair distribution functions (PDFs) of (i) an Ova Lavirun precipitate collected at OL9 (Fig. 1), (ii) AMD-titrated basaluminite obtained by titrating acid mine drainage, and (iii) synthetic Al_{13} sulfate are shown in Fig. 4. The diffraction pattern and PDF features of the Ova Lavirun precipitates are very similar to the AMD-titrated basaluminite sample, demonstrating that the samples from Ova Lavirun structurally are consistent with basaluminite as described by Carrero et al. (2017a). The PDF analysis further revealed a coherent domain size of ~1 nm in both samples, reflecting the nanocrystalline nature of these precipitates. In contrast, Al_{13} sulfate shows different PDF features as well as diffraction peaks, where only tetrahedral S-O and octahedral Al-O distance (1.45 Å and 1.88 Å, respectively) are clearly coincident in basaluminite as well

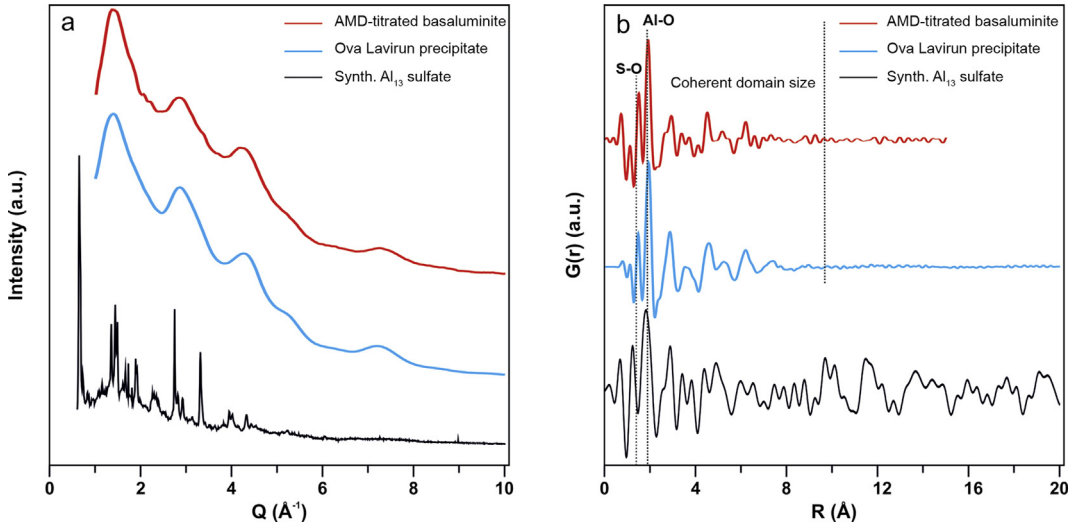

Fig. 4. (a) Synchrotron X-ray diffraction represented as scattering vector Q and (b) pair distribution function G(r) of (i) an Ova Lavirun precipitate, (ii) AMD-titrated basaluminite described by Carrero et al. (2017a), and (iii) synthetic Al_{13} sulfate precipitated from a solution with an Al/Si ratio of 12 and containing ca. 70% of Al_{13}.

as in Al_{13} sulfate. The mismatching PDF and the long coherent domain of Al_{13} sulfate confirm that basaluminite structurally differs from Al_{13} sulfate.

4.2.1.2. Infrared spectroscopy. The IR spectra of two Ova Lavirun precipitates collected at OL9 and OL11 are presented in Fig. 5 in comparison to synthetic basaluminite (Carrero et al., 2017a) and to synthetic Al_{13} sulfate. In general, all spectra show a low resolution reflecting a variety of local environments and disorder. The range of the stretching and bending modes of the SO_4^{2-} ions from 400 to 1200 cm^{-1} is characterized by two broad features, which can be decomposed into component bands using the second derivative. Due to the historical confusion regarding the nature of basaluminite (Carrero et al., 2017a), however, no unambiguous reference IR spectra exist for basaluminite. The reported IR spectra by Tien (1968) refers to "crystalline" basaluminite without any details to distinct bands or assignment and is hence distinct from the nanocrystalline precipitates from Ova Lavirun. Therefore, and because it represents the purest of our samples, band component analysis was exclusively done for the synthetic basaluminite spectrum in the fingerprint range of 400–1250 cm^{-1} (Fig. 6).

An undisturbed SO_4 group with tetrahedral symmetry (T_d) has 4 vibrational modes: $v_1 = 983\ cm^{-1}$, $v_2 = 450\ cm^{-1}$, $v_3 = 1105\ cm^{-1}$ and $v_4 = 611\ cm^{-1}$ (Nakamoto, 1986). Within mineral structures, however, the surrounding cations, OH groups, and H_2O molecules will distort the T_d symmetry of the sulfate anion. Distortion to C_{3v} symmetry lifts the degeneracy and 6 IR active modes are possible for one sulfate site (Adler and Kerr, 1965). Ross (1974), for instance, reports the following vibrational modes for the IR spectrum of potassium alum: $v_1 = 981\ cm^{-1}$, $v_2 = 465\ cm^{-1}$, $v_3 = 1105$ and $1200\ cm^{-1}$, and $v_4 = 600$ and $618\ cm^{-1}$. In contrast, our synthetic basaluminite sample

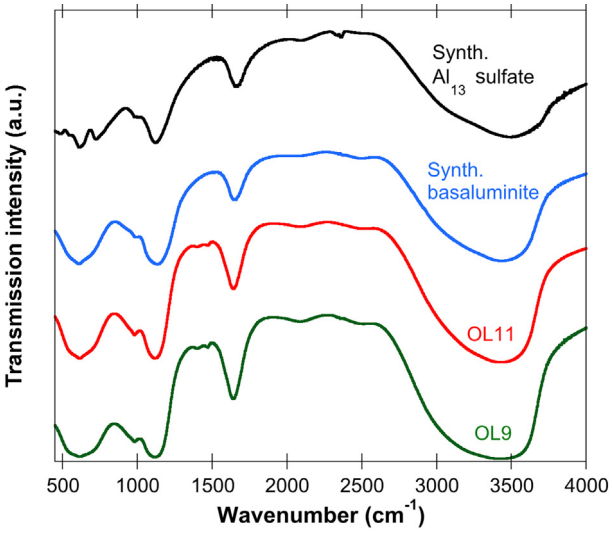

Fig. 5. Infrared spectra of two precipitates from Ova Lavirun (OL9, OL11), synthetic basaluminite described by Carrero et al. (2017a), and synthetic Al_{13} sulfate precipitated from a solution with an Al/Si ratio of 12 and containing ca. 70% of Al_{13}.

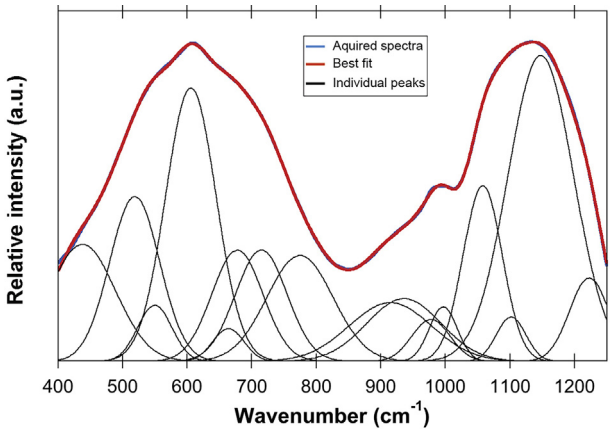

Fig. 6. Band component analysis of synthetic basaluminite in the region between 400 and 1250 cm^{-1}. Individual peaks correspond to the bonds of synthetic basaluminite listed in Table 3.

showed in the v_3 as well as in the v_4 region four modes of the SO_4 group (Fig. 6), suggesting yet a lower symmetry. Frost et al. (2013) discussed for the mineral creedite the lowering in symmetry by chelation and bridging of the sulfate to water molecules in the hydration sphere of the cations. The symmetry reduction results in splitting of the v_3 and v_4 modes into two components under C_{3v} and into three components under C_{2v} symmetry. More than three v_3 and v_4 modes suggest that both bidentate chelation and bidentate bridging occur. Such reduction in symmetry was also reported by Frost et al. (2015) for aluminite and the pseudo alums with the end members halotrichite and pickeringite (Reddy et al., 2006). All these minerals crystallize in the monoclinic crystal system like felsöbányaite (Farkas and Pertlik, 1997) and have a reduced symmetry of C_{2v} or less. Based on the four v_3 and four v_4 modes observed in the IR spectra such reduced symmetry also applies to our synthetic basaluminite sample (Figs. 5 and 6).

Taking into account the IR data summarized above and those of further Al-hydroxysulfates as listed in Table 3, our band component analysis (Fig. 6) results in the following interpretation of the synthetic basaluminite IR spectra (Table 3): the complex peak around 606 cm^{-1} can be resolved in $v_2(SO_4)$ bending modes at 438 and 550 cm^{-1}, an Al-O vibration at 519 cm^{-1} and a series of $v_4(SO_4)$ bending modes at 606, 664, 678, and 715 cm^{-1}. Modes at 775 and 915 cm^{-1}, as well as at 936 and 978 cm^{-1} were assigned to H_2O liberation and OH bending modes, respectively. A portion of the band at 775 cm^{-1} may be due to the Al-O stretching mode of the AlO_4 unit in polymerized aluminum. The peak around 1130 cm^{-1} comprises the $v_1(SO_4)$ symmetric stretching mode at 997 cm^{-1} and a series of $v_3(SO_4)$ asymmetric stretching modes at 1058, 1102, 1148, and 1223 cm^{-1}. Synthetic basaluminite further displays a water bending mode around 1640 cm^{-1}, water stretching modes at 3378, 3440, 3525, and 3549 cm^{-1} as well as OH stretching modes at 3480 and 3585 cm^{-1}.

The detailed comparison between the IR spectra for each sample type (i.e., Ova Lavirun precipitates, synth. basaluminite, synth. Al_{13} sulfate) reveals structural differences between Al_{13} sulfate and synthetic basaluminite,

Table 3
FTIR spectral data of vibrational modes and band assignment for precipitates from Ova Lavirun (six samples between OL9 and OL11), synthetic basaluminite, and synthetic Al_{13} sulfate.

[1]Precipitates (cm^{-1})	[1]Synth. basaluminite (cm^{-1})	[1]Synth. Al_{13} sulfate (cm^{-1})	[2]Al_{13} sulfate	Assignment	Minerals used for assignment	References
[3]428–431	n.a.	n.a.	n.a.	$\nu_2(SO_4)/\delta$(Si-O)	Alunite/kaolinite[5]	Lane (2007)/Madejova and Kommandel (2001)
n.a.	438	435	450	$\nu_2(SO_4)$	Pickeringite; Al_{13}-sulfate	Ross (1974); Kloprogge et al. (1992)
519–521	519	n.a.	491	Al-O	Alunite; Al_{13}-sulfate	Bishop and Murad (2005); Kloprogge et al (2001)
536–540	n.a.	536	n.a.	δ(Al-O-Si)/δ(OH)	Kaolinite/gibbsite	Vaculikova et al. (2011)/Elderfield (1973); Mönke (1962)
549–551	550	n.a.	552	$\nu_4(SO_4)/\nu_2(SO_4)$	Pickeringite/Al_{13} sulfate	Reddy et al. (2006)/Kloprogge et al. (2001)
608–612	606	606	610	$\nu_4(SO_4)$	Pickeringite; Al_{13} sulfate	Reddy et al. (2006); Kloprogge et al. (1992)
646–650	n.a.	648	n.a.	Si-O/Al-O	Kaolinite/Al_{13} sulfate	Vaculikova et al. (2011)/Kloprogge and Frost (1999)
n.a.	664	n.a.	n.a.	$\nu_4(SO_4)$	Aluminite; alunite	Frost et al. (2015); Murphy et al. (2009)
676–680	678	686	n.a.	$\nu_4(SO_4)$	Creedite; aluminite	Lane (2007); Frost et al. (2015)
713–718	715	725	715/723	$\nu_4(SO_4)/\nu(AlO_4)$	Halotrichite /Al_{13} sulfate	Reddy et al. (2006)/Kloprogge et al. (1992; 2001)
770–780	775	770	779	H_2O lib./$\nu(AlO_4)$	Creedite/Al_{13} sulfate	Lane (2007)/Schönherr and Bertram (1983); Kloprogge and Frost (1999)
910–912	915	n.a.	n.a.	δ(OH)	Kaolinite; mangazeite	Vaculikova et al. (2011); Chukanov and Chervonnyi (2016)
933–936	936	933	n.a.	δ(OH)	Kaolinite; mangazeite	Vaculikova et al. (2011); Chukanov and Chervonnyi (2016)
978–979	978	974	980	δ(OH)/δ(Al-OH)	Pickeringite/Al_{13} sulfate	Reddy et al. (2006)/Kloprogge et al. (1992; 2001)
997–1000	997	n.a.	990	$\nu_1(SO_4)$/Al-OH_2	Pickeringite/Al_{13} sulfate	Reddy et al. (2006)/Kloprogge et al. (1992; 2001)
1028–1029	n.a.	n.a.	n.a.	δ(OH)/ν(Si-O)	Gibbsite; alunite/kaolinite	Mönke (1962); Murphy et al. (2009)/Madejova and Kommandel (2001)
1059–1060	1058	n.a.	n.a.	$\nu_3(SO_4)$	Aluminite; halotrichite	Frost et al. (2015); Reddy et al. (2006)
1074–1078	n.a.	1087	1089	$\nu_3(SO_4)$	Halotrichite; Al_{13} sulfate	Reddy et al. (2006); Kloprogge et al. (1992, 2001)
1108–1114	1102	n.a.	1113	ν(Si-O)/$\nu_3(SO_4)$	Kaolinite/apjohnite; Al_{13} sulfate	Vaculikova et al. (2011)/Reddy et al. (2006); Kloprogge et al. (2001)
[4]1124–1126	n.a.	n.a.	n.a.	ν(Si-O)	Kaolinite	Madejova and Kommandel (2001)
1145–1150	1148	1138	1135	$\nu_3(SO_4)$	Pickeringite; Al_{13} sulfate	Reddy et al. (2006); Kloprogge et al. (1992)
[4]1222–1224	1223	n.a.	n.a.	$\nu_3(SO_4)$	Alunite	Murphy et al. (2009); Bishop and Murad (2005)
1430–1460	n.a.	n.a.	n.a.	$\nu(CO_3)$	Calcite	Huang and Kerr (1960)
1620–1640	1640	1640/1664	1639/1688	$\delta(OH)H_2O$	Crystal water	
≈2500	≈2500	n.a.	n.a.	$\nu(OH)H_2O$	Apjohnite; aluminite	Reddy et al. (2006); Frost et al. (2015)
3377–3379	3378	3400	3000	$\nu(H_2O)$	Gibbsite; mangazeite	Kloprogge et al. (2002); Chukanov and Chervonnyi (2016)
3440–3445	3440	3430	3434	$\nu(H_2O)$	Gibbsite; aluminite; creedite	Mönke (1962); Frost et al. (2013; 2015)
3475–3477	3480	3460	n.a.	ν(OH)	Alunite; apjohnite	Bishop and Murad (2005); Reddy et al. (2006)
3523–3525	3525	n.a.	n.a.	$\nu(H_2O)$	Gibbsite; aluminite; creedite	Kloprogge et al. (2002); Frost et al. (2013; 2015)
3545–3549	3549	3550	n.a.	$\nu(H_2O)$	Alunite	Bishop and Murad (2005)
3588–3590	3585	n.a.	n.a.	ν(OH)	Aluminite	Frost et al. (2015)
3610–3620	3613	3620	n.a.	ν(OH)	Kaolinite, gibbsite	Madejova and Kommandel (2001); Elderfield (1973)
3653–3654	n.a.	n.a.	n.a.	ν(OH)	Kaolinite	Madejova and Kommandel (2001)
3666–3669	n.a.	n.a.	n.a.	ν(OH)	Kaolinite	Madejova and Kommandel (2001)
3695–3697	n.a.	n.a.	n.a.	ν(OH)	Kaolinite	Madejova and Kommandel (2001)

ν_1: symmetric stretching modes.
ν_2: symmetric bending modes.
ν_3: asymmetric stretching modes.
ν_4: asymmetric bending modes.
ν(OH): O-H stretching modes.
δ(OH): O-H bending modes.
[1] Precipitates from Ova Lavirun (this study).
[2] Kloprogge et al. (1992, 2001), shown for comparison.
[3] Bands are determined by 2nd derivative. Based on small differences in the composition of the precipitates, the observed wavenumbers are characterized by the indicated ranges.
[4] not in all samples.
[5] kaolinite only refers to precipitates from Ova Lavirun.

particularly in the range of the v_3 and $v_4(SO_4)$ modes at 1000–1200 cm^{-1} (Table 3). Moreover, the Al-O stretching mode of the AlO_4 unit at about 724 cm^{-1} (Kloprogge et al., 1992; Bradley et al., 1993; Kloprogge et al., 2001; Liu and Zhao, 2009) is not identified in synthetic basaluminite, whereas it can be identified in synthetic Al_{13} sulfate (Table 3). In contrast, looking at the Ova Lavirun precipitates it becomes evident that the IR modes of synthetic basaluminite are completely reflected in the IR spectra of the natural precipitates. Additional to basaluminite, the natural precipitates show small bands of kaolinite and gibbsite. In summary, results from IR spectroscopy are consistent with the finding that the Ova Lavirun precipitates consist fundamentally of basaluminite.

4.2.1.3. NMR spectroscopy. The ^{27}Al MAS NMR spectra of two Ova Lavirun precipitates and synthetic Al_{13} sulfate are shown in Fig. 7. Both Ova Lavirun samples display a dominant and broad peak at about 7 ppm characteristic for Al[6] and a high degree of structural disorder typical for nanocrystalline phases. In contrast, only sample OL9 showed a detectable Al[4] peak at ca. 64 ppm corresponding to an Al[4] content of 2%. Such value is significantly lower than the 7.6% expected if the precipitates corresponded to an aggregation of Al_{13} only. Similarly, both samples show a distinct Al[5] peak at ca. 36 ppm corresponding to an Al[5] content of 2 and 6%, respectively, which was not observed in the reported NMR spectra of synthesized Al_{13} sulfates (Fig. 7, Ulrich and Pöthig, 2000) and Al_{13} gels (Furrer et al., 2002; Liu and Zhao, 2009). In contrast, analogous NMR results with distinct Al[5] peaks together with Al[6] and small Al[4] peaks were observed for natural and synthetic basaluminite (Carrero et al., 2017a), and during investigations of the buffering mechanism of acid mining lakes (Totsche et al., 2003). Obtained NMR spectra are hence fully consistent with a predominance of basaluminite in the Ova Lavirun precipitates.

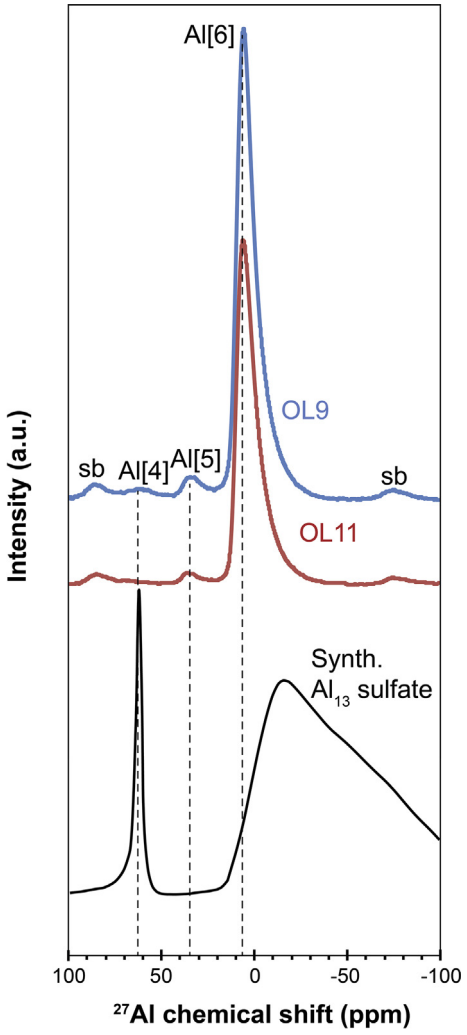

Fig. 7. NMR spectra of two precipitates from Ova Lavirun (OL9, OL11) and synthetic Al_{13} sulfate precipitated from a solution with an Al/Si ratio of 12 and containing ca. 70% of Al_{13}. The three peaks Al[4], Al[5] and Al[6] represent tetrahedral, five-coordinate, and octahedral aluminum, respectively. sb: side band.

The synthetic Al_{13} sulfate sample shows a strong and sharp Al[4] peak at ca. 63 ppm (Fig. 7) confirming the presence of substantial Al_{13}. The broad peak at about -15 ppm in the range of the Al[6] bonding sites is due to the presence of Si in the solution from which precipitation occurred (i.e., Al/Si = 12) or due to the presence of the δ-Al_{13} instead of the ε-Al_{13} isomer (Pilgrim et al., 2017).

4.2.2. Chemical characterization

The chemical composition of two precipitate samples is shown in Table 4. Both samples are dominated by H_2O + OH, Al, and SO_4 at very similar concentrations. The chemical composition is consistent with low-sulfate basaluminite, and the average concentration of both samples yields a stoichiometry of $Al_4(OH)_{10.43}(SO_4)_{0.79}{\cdot}2.2H_2O$, assuming that SO_4^{2-} and OH^- are interchangeable as suggested by Carrero et al. (2017b). The average Al/SO_4 ratio of 5.08 is higher than the one observed in basaluminite obtained by titration of AMD solutions (2.7–4.1; Totsche et al.,

Table 4
Chemical composition of precipitates collected at OL9 and OL11 (Fig. 1) during the July 2016 sampling campaign. Also shown is the theoretical composition of the inferred basaluminite stoichiometry.

		OL9	OL11	$Al_4(OH)_{10.43}(SO_4)_{0.79}{\cdot}2.2H_2O$
OH + H_2O	wt%	54.35	53.27	54.15
Al	wt%	26.72	27.09	26.96
SO_4	wt%	18.52	19.20	18.89
Si	wt%	0.13	0.20	0.0
Fe	µg/g	985	1107	0.0
As	µg/g	636	415	0.0
Ca	µg/g	144	112	0.0
K	µg/g	121	105	0.0
Mg	µg/g	206	180	0.0
Na	µg/g	60	82	0.0
Zn	µg/g	43	59	0.0
Ni	µg/g	<20	<20	0.0
Cu	µg/g	72	44	0.0
Mn	µg/g	<20	<20	0.0
Sr	µg/g	<20	<20	0.0
Al/SO_4	mol ratio	5.14	5.02	5.08

2003; Sánchez-España et al., 2011; Carrero et al., 2015, 2017b), but similar to the ratio observed in basaluminite that have precipitated from neutralized streams at AMD sites (Nordstrom et al., 1984; Ball and Nordstrom, 1989; Bigham and Nordstrom, 2000). Both basaluminite samples are further characterized by elevated Fe and As concentrations up to 1110 and 640 μg/g, respectively, whereas other metals are at background concentrations only.

5. DISCUSSION

5.1. Al solubility control and kinetics of basaluminite precipitation

To assess the controlling parameters of basaluminite precipitation along Ova Lavirun, the ion activity product *IAP* of the proposed basaluminite stoichiometry ($Al_4(OH)_{10.43}(SO_4)_{0.79}{\cdot}2.2H_2O$) was calculated in combination with our speciation calculations:

$$\log(IAP) = 4\log(a_{Al^{3+}}) + 0.79\log(a_{SO_4}) + 10.43pH \quad (2)$$

With the exception of Sample OL11 collected in July 2016 and affected by the Western fork of Ova Lavirun, all samples from the section with visible precipitates (OL9–OL15, Fig. 1) yield basaluminite log(*IAP*) values within a rather narrow range of 32.3–33.3 (Table 1, Fig. 3d). For these samples, our speciation calculations predict a minor Al_{13} content of ≤20% (Fig. 3d), which is consistent with the minor contribution inferred from the Al speciation analysis using the kinetic Ferron method. In contrast, no Al_{13} is predicted for the samples collected upstream of the occurrence of the precipitates (OL1–OL8). At first, the quasi-constant basaluminite log(*IAP*) values seem remarkable, given the large variation in pH and SO_4 and Al concentration of these samples (pH: 5.2–7.3; SO_4: 82–220 mg/L; Al: 0.05–4.4 mg/L), as well as the variable discharge conditions observed during the two sampling campaigns. Eq. (2), however, demonstrates that calculated log(*IAP*) values are strongly sensitive to the pH value, whereas due to Al speciation they are much less sensitive to dissolved Al concentrations. Accordingly, if log(*IAP*) values calculated for OL15 are not considered due to their rather low Al concentrations (0.048 and 0.207 mg/L), the pH-, and SO_4 and Al concentration ranges with quasi-constant log(*IAP*) values is significantly smaller (pH: 5.2–5.9; SO_4: 94–220 mg/L; Al: 0.53–4.4 mg/L).

The main implication of observing of a quasi-constant log(*IAP*) value is that such value actually equalizes the logarithm of the basaluminite equilibrium constant (log(*K*)) at the given sampling temperature (4–8.5 °C). Moreover, it confirms earlier findings that the pH-dependent solubility of basaluminite or other Al-hydroxysulfates exert a strong control on the dissolved Al concentration (e.g., Nordstrom, 1982; Jones et al., 2011).

The strong solubility control by basaluminite is further demonstrated by mixing calculations performed for the first basaluminite occurrence where OL8 is merged with T4 to form OL 9 (Fig. 1). Assuming that SO_4 behaves more or less conservatively in relation to Al yields numerically determined mixing proportions of 69:31 and 68:32 for the two sampling campaigns at this particular confluence point. Table 5 shows that such conservative mixing can well

Table 5
Comparison of measured and calculated Al, Mg, and SO_4 concentrations at the first basaluminite occurrence at OL9 where Ova Lavirun (OL8) merges with T4 (Fig. 1). The imbalance of the Al budget (considering conservative mixing) and the amounts of instantaneous basaluminite precipitation predicted by PHREEQC are shown for both sampling campaigns.

			OL8	T4	OL9		
					Measurement	[1]Conservative mixing calculation	[2]Mixing calculations including basaluminite precipitation
Sep. 2015	pH	–	5.05	6.69	5.45	n.a.	5.47
	Al	mg/L	3.3	<0.003	1.76	2.28	1.72
	SO_4	mg/L	234	9.2	165	164.76	164.42
	Mg	mg/L	35.2	0.65	26.10	24.56	24.56
	[3]Mixing proportion	fraction	0.692	0.308	n.a.	n.a.	n.a.
	Al overestimation	%	n.a.	n.a.	n.a.	29.8	n.a.
	[4]Basaluminite prec.	μmol/L	n.a.	n.a.	n.a.	n.a.	5.21
July 2016	pH	–	4.92	6.42	5.29	n.a.	5.30
	Al	mg/L	2.55	<0.003	1.60	1.75	1.53
	SO_4	mg/L	134.6	4.85	93.8	93.73	93.59
	Mg	mg/L	20.67	0.37	14.58	14.28	14.28
	[3]Mixing proportion	fraction	0.685	0.315	n.a.	n.a.	n.a.
	Al overestimation	%	n.a.	n.a.	n.a.	9.4	n.a.
	[4]Basaluminite prec.	μmol/L	n.a.	n.a.	n.a.	n.a.	2.08

[1] Calculated assuming that SO_4^{2-} behaves conservatively in relation to Al.
[2] Obtained from geochemical modeling using PHREEQC (in- and output files are provided as Electronic Annexes).
[3] Determined numerically assuming that SO_4 behaves conservatively during mixing (SO_4 conc. of calculated conservative mixture has to match SO_4 concentration observed at OL9).
[4] Calculated by PHREEQC by forcing the saturation index of basaluminite to 0, whereas the actual basaluminite log(*K*) was set to the log (*IAP*) determined for Sample OL9 during the corresponding sampling campaign (Table 1).

explain the concentrations of the major cation (Mg) and anion (SO_4), whereas the Al concentration is overestimated by 10–30%. Since the two Ova Lavirun samples at OL8 and OL9 are physically separated by about 50 m only (Fig. 1), such Al overestimation demonstrates that basaluminite precipitation occurs almost instantaneously when the pH increases to about 5.4 upon mixing with tributary T4. Fast precipitation is further in agreement with (i) the observation that after mixing and initial basaluminite precipitation at OL9 the chemical composition of Ova Lavirun remains constant unless it does not merge with the next tributary (e.g. Sample OL10, Fig. 3b), (ii) the nanocrystalline occurrence of basaluminite (Fig. 4b), and (iii) PHREEQC calculations, which nicely reconstruct the pH value measured at OL9, when numerically mixing OL8 and T4 and simultaneously allowing basaluminite to precipitate (Table 5). The later was simulated by forcing the basaluminite saturation index to 0, whereas the actual basaluminite log(K) was set to the log(IAP) values determined for Sample OL9 during the corresponding sampling campaigns (Table 1). In contrast to pH, Al concentrations predicted by the PHREEQC mixing calculations do not perfectly match the observed concentration at OL9 (Table 5) because basaluminite log (IAP) values are not highly sensitive to dissolved Al concentrations as discussed above.

5.2. Temperature dependence of the basaluminite log(K)

To the best of our knowledge, the log(K) value of basaluminite has only been determined at 25 °C and for an ideal stoichiometry of $Al_4(OH)_{10}(SO_4)\cdot 5H_2O$, and reported values range between 22 and 24 (Singh and Brydon, 1969; Adams and Rawajfih, 1977; Sánchez-España et al., 2011). Interestingly, the log(K) inferred for basaluminite from Ova Lavirun at T = 4–8.5 °C is up to 11 orders of magnitude higher (log(K) ≈ 33). The discrepancy is partially inherited from considering the inferred ($Al_4(OH)_{10.43}(SO_4)_{0.79}\cdot 2.2H_2O$) instead of the ideal basaluminite stoichiometry ($Al_4OH_{10}(SO_4)\cdot 5H_2O$), but this can only account for a difference of 3–4 orders of magnitude (Table 1). Accordingly, the log(K) of basaluminite seems to be strongly temperature dependent, which can be expressed by integration of the Van't Hoff equation (Sanjuan et al., 2014)

$$\log(K)_T = \log(K)_{298} - \frac{\Delta H_R^{\circ}}{2.303 \cdot R} \cdot \left(\frac{1}{T} - \frac{1}{298}\right) \quad (3)$$

where K_{298} refers to the equilibrium constant at 25 °C, $\Delta H°_R$ is the standard molar enthalpy of reaction (J mol^{-1}), T is the temperature given in K, and R refers to the ideal gas constant (8.3143 J K^{-1} mol^{-1}). Applying Eq. (3) with the average temperature observed along the Ova Lavirun section with visible precipitates (T = 6.8 °C), the corresponding average log(IAP) value referring to the ideal basaluminite stoichiometry ($\log(K)_T = 29.73$, Table 1), and the average basaluminite log(K) reported at 25 °C ($\log(K)_{298} = 23.58$) yields an enthalpy of reaction of −539 kJ/mol.

To date, calorimetric investigations on Al-hydroxysulfates similar to basaluminite were so far only conducted on alunite ($KAl_3(SO_4)_2(OH)_6$, Bohmhammel et al., 1987) and $Na(AlO_4)Al_{12}(OH)_{24}(H_2O)_{12}(SO_4)_4$, which refers to crystalline Al_{13} sulfate (Armstrong et al., 2011). Therefore, in any of the PHREEQC databases enthalpies of reaction of Al-hydroxysulfates similar to basaluminite are tabulated for alunite only. The values listed in the WATEQ4F/PHREEQC and LLNL databases are −210 and −232 kJ mol^{-1}, respectively, which is less than half the value calculated for basaluminite above. Given that alunite does usually not simultaneously form with basaluminite (Bigham and Nordstrom, 2000) and that we could not use the basaluminite stoichiometry inferred from the chemical analysis (Table 4) to estimate $\Delta H°_R$, however, such discrepancy seems plausible and hence supports the proposed temperature dependence of the basaluminite log(K) value. Moreover, a strongly negative enthalpy of reaction is supported by calorimetric investigations of crystalline Al_{13}-bearing sulfate ($Na(AlO_4)Al_{12}(OH)_{24}(H_2O)_{12}(SO_4)_4$), yielding an enthalpy of reaction of −944.30 ± 5.66 kJ mol^{-1} for the dissolution in 5 N HCl at 301 K (Armstrong et al., 2011). In any case, additional investigations are required to quantify the temperature dependence of the basaluminite log(K) value.

5.3. Factors potentially controlling basaluminite precipitation

Despite the observation that the precipitates from Ova Lavirun structurally refer to basaluminite, NMR spectroscopy (Fig. 7), the kinetic Ferron method, as well as geochemical speciation calculations (Fig. 3c) provide multiple evidences for the simultaneous occurrence of minor amounts of Al_{13}. The coexistence of Al_{13} and basaluminite has been inferred previously (Carrero et al., 2017a). Due to the fact that the analyzed precipitates represent time-integrated properties whereas the streamwater samples refer to one point in time, however, further experimental studies are required to quantitatively assess whether the formation Al_{13} and basaluminite are related or if their simultaneous occurrence is fortuitous only. The same applies for elucidating why the precipitates from Ova Lavirun refer dominantly to basaluminite rather than to an aggregation of Al_{13} such as postulated for virtually the same setting of acidic stream neutralization (Ulrich and Pöthig, 2000; Furrer et al., 2002). Nevertheless, the consistency of our data allows presenting the following hypotheses on the fate of Al_{13} and its potential role in controlling basaluminite precipitation.

According to geochemical speciation calculations performed for the Al-H_2O system, at Al concentrations similar to the one observed along the upper part of Ova Lavirun (>2.5 mg/L; ~0.1 mmol/L) Al_{13} becomes a significant Al species at a pH > 4.8 (Furrer et al., 1992b). From the synthesis of Al_{13}-bearing sulfate crystals (Johansson, 1960, 1963; Armstrong et al., 2011), however, it is known that Al_{13} tends to precipitate in the presence of sulfate anions. Based on these considerations it is possible that Al_{13} forms when Ova Lavirun is for the first time neutralized to a

pH > 5 upon mixing with tributary T4 such as suggested with our geochemical speciation calculations (Fig. 3d), but that significant accumulation is limited by sulfate concentrations >100 mg/L due to immediate precipitation of Al_{13}-bearing sulfates. Such interpretation is consistent with our speciation calculations suggesting that the $AlSO_4^+$ complex is an important Al species (Table 1), which can potentially limit the formation of Al_{13}. Moreover, Allouche and Taulelle (2003) have shown that the presence of F^- ions hinders the formation of Al_{13} while promoting the one of Al_{30} instead. Hence, the formation of Al_{13} may be also limited due to F concentrations up to 2 mg/L along the section with visible precipitates, which is consistent with our speciation calculations, suggesting that along this section AlF_2^+ and AlF^{2+} account for up to 76% of total dissolved Al (Table 1). Finally, our speciation calculations predict lower Al_{13} contents than the ones obtained when performing the speciation calculations at the same pH but at 25 °C (Table 1). As a consequence, low water temperatures observed in Ova Lavirun have the potential to limit the accumulation of Al_{13} as well.

In the literature it is well accepted that so called pre-nucleation clusters may form precursors for the precipitation of XRD amorphous as well as crystalline phases (Gebauer et al., 2014, and references therein). Typical example include the formation of pre-nucleation calcium carbonate clusters prior calcium carbonate precipitation (Gebauer et al., 2008), the formation of mono- or di-nuclear iron-hydroxide species prior to the formation of amorphous Fe-oxyhydroxides (Cornell et al., 1989), and the polymerization of silica monomer forming amorphous silica eventually (Perry and Keeling-Tucker, 2000). In case of Al_{13} it has been shown that Al_{13} can form a precursor for the precipitation of crystalline Al-hydroxides (Bottero et al., 1987; Bradley et al., 1993). Due to its rather high stability, however, Al_{13} may not fully qualify as a pre-nucleation cluster (Gebauer et al., 2014). Nevertheless, the simultaneous occurrence of basaluminite and Al_{13} in our samples as well as our speciation calculations suggests that aqueous Al_{13} and/or Al_{13}-bearing sulfates may be related to the subsequent precipitation of basaluminite. Such hypothesis is consistent with the rather large pH range for which basaluminite precipitation has been described in the literature, and the fact that the formation pH of aqueous Al_{13} is negatively correlated to the dissolved total Al concentration (Furrer et al., 1992b). For instance, in the studies where basaluminite was synthesized by titrating acid mine drainage solutions, precipitation occurred between pH 4.2 and 4.7 at Al concentrations >100 mg/L (i.e., 3 mmol/L) (Sánchez-España et al., 2011; Carrero et al., 2015, 2017b). In contrast, along Ova Lavirun basaluminite precipitation occurs at Al concentrations <2 mg/L (<0.075 mmol/L) at a pH > 5.3. Hence, the formation of basaluminite may depend on the first formation of aqueous Al_{13} during neutralization of Al- and sulfate-rich acidic solutions. Due to the high amount of transitional polymers observed in streamwater samples collected along the section with visible precipitates (OL13–OL15, Table 2), however, it is also possible that the precipitation of basaluminite builds on Al polymers of unknown structure rather than on Al_{13}.

5.4. Basaluminite is a highly efficient sink for As

Despite the low pH and high sulfate concentrations, dissolved arsenic concentrations of Ova Lavirun are rather low. For the September 2015 sampling campaign they were all below the detection limit of 0.01 mg/L, whereas in July 2016 they gradually decreased from 0.115 mg/L at OL4 to 0.011 at OL14 (Table 1). The low As concentrations are due to the fact that pyrite-bearing chlorite mica-schists exposed at the origin of Ova Lavirun are almost As-free (Ghebremedhin, 2017). Similarly, the observation that other heavy metal concentrations are mildly elevated only (e.g., Zn, Ni, Mn; Tables S1 and S2, Electronic Annex) is due to the limited occurrence of other metal sulfides than pyrite. Given the low dissolved As concentrations, the elevated As content of the collected basaluminite samples (Table 4) is remarkable and confirms the high affinity for As under field-scale conditions (Carrero et al., 2015, 2017b). Although we cannot rule out elevated dissolved As concentrations during specific discharge events, our analyses suggest that with time basaluminite can strongly concentrate As with respect to the solution from which it precipitates, and thus has the potential to almost completely remove As in aqueous environments.

The uptake of As by basaluminite has been attributed to its layered structure where sulfate anions are arranged as an interlayer connecting positively charged Al-octahedron layers (Carrero et al., 2017a, 2017b). These studies thus suggest that sulfate anions are easily exchangeable and that the affinity for arsenate anions ($H_2AsO_4^-$) as well as for selenate (SeO_4^{2-}) is high. At our study site, the anion exchange capacity of basaluminite is not only manifested by elevated As concentrations but also by the rather high Al/SO_4 ratio of 5.1 (Table 4) and the elevated formation pH (>5.3, Fig. 3b), suggesting a positive correlation between the Al/SO_4 ratio and the formation pH. This is because such correlation is consistent with a substitution reaction where one sulfate anion is replaced by two hydroxide ions, which is favored with increasing pH due to the subsequent increase in hydroxide activity. In contrast, in the studies where basaluminite was synthesized by titrating acid mine drainage solutions, the low Al/SO_4 ratio (2.7–4.1) coincides with a low basaluminite formation pH of 4.2–4.7 (Totsche et al., 2003; Sánchez-España et al., 2011; Carrero et al., 2015, 2017b), indicating that basaluminite serves as a strong anion exchanger. However, more research is required to investigate whether the mobility of toxic oxyanions other than arsenate and selenate could be reduced in the presence of basaluminite, in order to further test its performance in conjunction with treatment systems for acid waters.

6. SUMMARY AND CONCLUSIONS

We have presented an extended geochemical dataset from a large occurrence of nanocrystalline Al-hydroxysulfates that form naturally in a small alpine catchment in Switzerland when an acidic mountainous stream (pH ~ 4) is neutralized by mixing with several neutral tributaries. The collected data include streamwater analysis,

synchrotron based high-energy X-ray diffraction analysis, nuclear magnetic resonance and infrared spectroscopy, as well as results from geochemical modeling. The main conclusions are:

1. Structurally, the investigated Al-hydroxysulfates refer dominantly to basaluminite rather than to an aggregation of the ε-Keggin polyoxocation $[Al_{12}(AlO_4)(OH)_{24}(H_2O)_{12}]^{7+}$ (Al_{13}) such as postulated for virtually the same setting of acidic stream neutralization (Furrer et al., 2002). Geochemical speciation calculations suggest that the formation of Al_{13} is limited by low temperature (4–8 °C) and relatively high concentrations of sulfate and fluoride on the order of 100 and 1–2 mg/L, respectively.
2. Based on the coexistence of minor amounts of Al_{13} with basaluminite in the precipitates, geochemical speciation calculations and the observed basaluminite formation pH (>5), it is hypothesized that the formation of basaluminite builds on the initial formation of the Al_{13} polymer or on Al polymers of unknown structure.
3. Basaluminite precipitation occurs instantaneous and exerts a strong solubility control on dissolved Al concentrations. Fast precipitation is one of the reasons for the nanocrystalline character of basaluminite.
4. Basaluminite forms a highly efficient sink for As, confirming the reported affinity for arsenate anions ($H_2AsO_4^-$) (Carrero et al., 2017a). The positive correlation between the formation pH and the Al/SO_4 ratio further demonstrates that basaluminite operates as an efficient anion exchanger. This suggests that basaluminite may reduce the mobility of other toxic oxyanions as well and emphasizes its important role in conjunction with the treatment of acid waters.

ACKNOWLEDGMENTS

We thank Claudio Bazzell and Nadia Federspiel for telling us about the large and intriguing occurrence of basaluminite precipitates in the Engadin Valley. Dawit Ghebremedhin is acknowledged for assistance in the field. Analytical support during chemical analysis of streamwater samples and basaluminite precipitated by Priska Bähler and Nick Waber are greatly appreciated. We thank Martin Fisch for his help with TOPAS. Finally, we thank the Spanish Ministry of Economy, Industry and Competitiveness (ERAMIN; PCIN2015-242-256) for financial research support. Comments of three anonymous reviewers and the Associate Editor, Jeff Catalano, helped to greatly improve the quality of the manuscript.

APPENDIX A. SUPPLEMENTARY MATERIAL

Supplementary data associated with this article can be found, in the online version, at https://doi.org/10.1016/j.gca.2018.06.031.

REFERENCES

Adams F. and Rawajfih Z. (1977) Basaluminite and alunite: a possible cause of sulfate retention by acid soils. *Soil. Sci. Soc. Am. J.* **41**, 686–692.

Adler H. H. and Kerr P. F. (1965) Variations in infrared spectra, molecular symmetry, and site symmetry of sulfate minerals. *Am. Mineral.* **50**, 132–147.

Allouche L., Gérardin C., Loiseau T., Férey G. and Taulelle F. (2000) Al_{30}: a giant aluminum polycation. *Angew. Chem. Int. Ed.* **39**, 511–514.

Allouche L. and Taulelle F. (2003) Fluorination of the ε-Keggin Al_{13} polycation. *Chem. Commun.*, 2084–2085.

Armstrong C. R., Casey W. H. and Navrotsky A. (2011) Energetics of Al_{13} Keggin cluster compounds. *P. Natl. Acad. Sci.* **108**, 14775–14779.

Ball J. W. and Nordstrom D. K. (1989) Final revised anaylyses of major and trace elements from acid mine waters in the Leviathan mine drainage basin, California and Nevada—October 1981 to October 1982. *U.S. Geol. Survey Water-Res. Invest. Rep.* **89–4138**, 49p.

Ball J. W. and Nordstrom D. K. (1991) WATEQ4F—User's manual with revised thermodynamic data base and test cases for calculating speciation of major, trace and redox elements in natural waters. *U.S. Geol. Survey Open-File Rep.* **90–129**, 185p.

Bannister F. A. and Hollingworth S. E. (1948) Two new British minerals. *Nature* **162**, 565.

Bertram R., Geßner W., Müller D. and Danner M. (1994) Characterization of Al(III) species in basic aluminium chloride flocculants by means of ferron method and ^{27}Al nuclear magnetic resonance. *Acta Hydroch. Hydrob.* **22**, 265–269.

Bertram R., Stieber E. and Geßner W. (1996) Toxizität von aluminium – Al Species in protolysierten aluminiumchloridlösungen. *Umweltchem. Ökotox.* **8**, 78–82.

Bigham J. M. and Nordstrom D. K. (2000) Iron and aluminum hydroxysulfates from acid sulfate waters. *Rev. Mineral. Geochem.* **40**, 351–403.

Bishop J. L. and Murad E. (2005) The visible and infrared spectral properties of jarosite and alunite. *Am. Mineral.* **90**, 1100–1107.

Bohmhammel K., Naumann R. and Paulik F. (1987) Thermoanalytical and calorimetric investigations on the formation and decomposition of some alunites. *Thermochim. Acta* **121**, 109–119.

Bottero J. Y., Axelos M., Tchoubar D., Cases J. M., Fripiat J. J. and Fiessinger F. (1987) Mechanism of formation of aluminum trihydroxide from keggin Al13 polymers. *J. Colloid. Interf. Sci.* **117**, 47–57.

Bradley S. M., Kydd R. A. and Howe R. F. (1993) The structure of Al gels formed through the base hydrolysis of Al^{3+} aqueous solutions. *J. Colloid. Interf. Sci.* **159**, 405–412.

Bucher K., Zhou W. and Stober I. (2017) Rocks control the chemical composition of surface water from the high Alpine Zermatt area (Swiss Alps). *Swiss J. Geosci.* **110**, 811–831.

Carrero S., Pérez-López R., Fernandez-Martinez A., Cruz-Hernández P., Ayora C. and Poulain A. (2015) The potential role of aluminium hydroxysulphates in the removal of contaminants in acid mine drainage. *Chem. Geol.* **417**, 414–423.

Carrero S., Fernandez-Martinez A., Perez-Lopez R., Lee D., Aquilanti G., Poulain A., Lozano A. and Nieto J. M. (2017a) The nanocrystalline structure of basaluminite, an aluminum hydroxide sulfate from acid mine drainage. *Am. Mineral.* **102**, 2381–2389.

Carrero S., Fernandez-Martinez A., Pérez-López R., Poulain A., Salas-Colera E. and Nieto J. M. (2017b) Arsenate and selenate scavenging by basaluminite: insights into the reactivity of

aluminum phases in acid mine drainage. *Environ. Sci. Technol.* **51**, 28–37.

Changui C., Stone W. E. E., Vielvoye L. and Dereppe J.-M. (1990) Characterization by nuclear magnetic resonance spectroscopy, ferron assay, and acidification of partially neutralized aluminium solutions. *J. Chem. Soc., Dalton* **Trans**, 1723–1726.

Chukanov N. V. and Chervonnyi A. D. (2016) *Infrared Spectroscopy of Minerals and Related Compounds*. Springer, Cham.

Coelho A. A. (2016) *TOPAS-Acedemic Version 6*. Coelho Software, Brisbane, Australia.

Cornell R. M., Giovanoli R. and Schneider W. (1989) Review of the hydrolysis of iron(III) and the crystallization of amorphous iron(III) hydroxide hydrate. *J. Chem. Technol. Biot.* **46**, 115–134.

Elderfield H. (1973) The development of crystalline structure in aluminium hydroxide polymorphs on ageing. *Mineral. Mag.* **39**, 89–96.

Evangelou V. P. and Zhang Y. L. (1995) A review: Pyrite oxidation mechanisms and acid mine drainage prevention. *Crit. Rev. Environ. Sci. Technol.* **25**, 141–199.

Farkas L. and Pertlik F. (1997) Crystal structure determinations of felsöbányaite and basaluminite, $Al_4(SO_4)(OH)_{10}x4H_2O$. *Acta Mineral. Szeged* **38**, 5–15.

FOEN, 2016. Swiss Federal Office for the Environment: Discharge and waterlevel measurements in the Chamuerabach La Punt-Chamues-ch <http://www.hydrodaten.admin.ch/en/2263.html>.

Frost R. L., Xi Y., Scholz R., López A. and Granja A. (2013) Infrared and Raman spectroscopic characterisation of the sulphate mineral creedite – $Ca_3Al_2SO_4(F, OH)\cdot 2H_2O$ – and in comparison with the alums. *Spectrochim. Acta A* **109**, 201–205.

Frost R. L., López A., Scholz R. and Wang L. (2015) A Raman and infrared spectroscopic study of the sulphate mineral aluminite $Al_2(SO_4)(OH)_4\cdot 7H_2O$. *Spectrochim. Acta A* **148**, 232–236.

Furrer G., Ludwig C. and Schindler P. W. (1992a) On the chemistry of the Keggin Al_{13} polymer: I acid-base properties. *J. Colloid. Interf. Sci.* **149**, 56–67.

Furrer G., Trusch B. and Müller C. (1992b) The formation of polynuclear Al_{13} under simulated natural conditions. *Geochim. Cosmochim. Acta* **56**, 3831–3838.

Furrer G., Phillips B. L., Ulrich K.-U., Pöthig R. and Casey W. H. (2002) The origin of aluminum flocs in polluted streams. *Science* **297**, 2245–2247.

Gebauer D., Völkel A. and Cölfen H. (2008) Stable prenucleation calcium carbonate clusters. *Science* **322**, 1819–1822.

Gebauer D., Kellermeier M., Gale J. D., Bergstrom L. and Colfen H. (2014) Pre-nucleation clusters as solute precursors in crystallisation. *Chem. Soc. Rev.* **43**, 2348–2371.

Ghebremedhin D. (2017) *Origin and fate of acidic surface waters: a case study from the Engadine Valley* MSc thesis. University of Bern, Switzerland.

Huang C. K. and Kerr P. F. (1960) Infrared study of the carbonate minerals. *Am. Mineral.* **445**, 311–324.

Jäckli H. (1970) Kriterien zur Klassifikation von Grundwasservorkommen. *Eclogae Geol. Helv.* **63**(2), 389–434.

Johansson G. (1960) On the crystal structure of some basic aluminium salts. *Acta Chem. Scand.* **14**, 771–773.

Johansson G. (1963) On the crystal structure of basic aluminium sulfate 13 $Al_2O_3\cdot 6SO_3\cdot xH_2O$. *Ark. Kemi* **20**, 321–342.

Jones A. M., Collins R. N. and Waite T. D. (2011) Mineral species control of aluminum solubility in sulfate-rich acidic waters. *Geochim. Cosmochim. Acta* **75**, 965–977.

Juhas P., Davis T., Farrow C. L. and Billinge S. J. L. (2013) PDFgetX3: a rapid and highly automatable program for processing powder diffraction data into total scattering pair distribution functions. *J. Appl. Crystallogr.* **46**, 560–566.

Kieffer J. and Karkoulis D. (2013) PyFAI, a versatile library for azimuthal regrouping. *J. Phys. Conf. Ser.* **425** 202012.

Kim Y. (2015) Mineral phases and mobility of trace metals in white aluminum precipitates found in acid mine drainage. *Chemosphere* **119**, 803–811.

Kloprogge J. T., Geus J. W., Jansen J. B. H. and Seykens D. (1992) Thermal stability of basic aluminum sulfate. *Thermochim. Acta* **209**, 265–276.

Kloprogge J. T. and Frost R. L. (1999) Raman and infrared spectroscopic investigation of the neutralisation of aluminium in the presence of monomeric orthosilicic acid. *Spectrochim. Acta A* **55**, 1359–1369.

Kloprogge J. T., Ruan H. and Frost R. L. (2001) Near-infrared spectroscopic study of basic aluminum sulfate and nitrate. *J. Mater. Sci.* **36**, 603–607.

Kloprogge J. T., Ruan H. D. and Frost R. L. (2002) Thermal decomposition of bauxite minerals: infrared emission spectroscopy of gibbsite, boehmite and diaspore. *J. Mater. Sci.* **37**, 1121–1129.

Lane Melissa D. (2007) Mid-infrared emission spectroscopy of sulfate and sulfate-bearing minerals. *Am. Mineral.* **92**, 1–18.

Lee G., Bigham J. M. and Faure G. (2002) Removal of trace metals by coprecipitation with Fe, Al and Mn from natural waters contaminated with acid mine drainage in the Ducktown Mining District, Tennessee. *Appl. Geochem.* **17**, 569–581.

Liu J. and Zhao F. (2009) Characterization of arsenate adsorption on amorphous Al gels with Keggin structure by Fourier transformed infrared spectroscopy and MAS ^{27}Al NMR. *Chin. J. Geochem.* **28**, 61–69.

Madejova J. and Komadel P. (2001) Baseline studies of the clay minerals society source clays: infrared methods. *Clay Clay Miner.* **49**, 410–432.

Mertens J., Rose J., Kägi R., Chaurand P., Plötze M., Wehrli B. and Furrer G. (2012) Adsorption of arsenic on polyaluminum granulate. *Environ. Sci. Technol.* **46**, 7310–7317.

Moenke H. (1962) *Mineralspektren*. Akademieverlag, Berlin.

Munk L., Faure G., Pride D. E. and Bigham J. M. (2002) Sorption of trace metals to an aluminum precipitate in a stream receiving acid rock-drainage; Snake River, Summit County, Colorado. *Appl. Geochem.* **17**, 421–430.

Murphy P. J., Smith A. M. L., Hudson-Edwards K. A., Dubbin W. E. and Wright K. (2009) Raman and IR spectroscopic studies of alunite-supergroup compounds containing Al, Cr^{3+}, Fe^{3+} and V^{3+} at the *B* site. *Can Mineral.* **47**, 663–681.

Nakamoto K. (1986) *Infrared and Raman Spectra of Inorganic and Coordination Compounds*. John Wiley, New York.

Nordstrom D. K. (1982) The effect of sulfate on aluminum concentrations in natural waters: some stability relations in the system Al_2O_3-SO_3-H_2O at 298 K. *Geochim. Cosmochim. Acta* **46**, 681–692.

Nordstrom D. K., Ball J. W., Roberson C. E. and Hanshaw B. B. (1984) The effect of sulfate on aluminum concentrations in natural waters. II. Field occurrences and identification of aluminum hydroxysulfate precipitates. *Geol. Soc. Am. Program Abstr.* **16**, 611.

Parker D. R. and Bertsch P. M. (1992) Identification and quantification of the "Al_{13}" tridecameric aluminum polycation using ferron. *Environ. Sci. Technol.* **26**, 908–914.

D.L. Parkhurst C.A.J. Appelo (2013) Description of input and examples for PHREEQC version 3—a computer program for speciation, batch-reaction, one-dimensional transport, and inverse geochemical calculations. U.S. Geol. Surv. Tech. Methods book 6, chap. A43, 497 p. Available only at http://pubs.usgs.gov/tm/406/a443

Perry C. C. and Keeling-Tucker T. (2000) Biosilicification: the role of the organic matrix in structure control. *J. Biol. Inorg. Chem.* **5**, 537–550.

Peters T. (2005) Geologischer Atlas der Schweiz (1:25000), Erläuterung Atlasblatt 118. *Bundesamt für Wasser und Geologie*, 96p.

Pilgrim C. D., Callahan J. R., Colla C. A., Ohlin C. A., Mason H. E. and Casey W. H. (2017) ^{27}Al MQMAS of the δ-Al^{13}-Keggin. *Dalton Trans.* **46**, 2249–2254.

Plyasunov A. V. and Grenthe I. (1994) The temperature dependence of stability constants for the formation of polynuclear cationic complexes. *Geochim. Cosmochim. Acta* **58**, 3561–3582.

Prietzel J. and Hirsch C. (1998) Extractability and dissolution kinetics of pure and soil-added synthesized aluminium hydroxy sulphate minerals. *Eur. J. Soil Sci.* **49**, 669–681.

Reddy L. S., Reddy S. G., Wain D. L., Martens W. N., Reddy J. B. and Frost R. L. (2006) Electron paramagnetic resonance, optical absorption and IR spectroscopic studies of the sulphate mineral apjohnite. *Spectrochim. Acta A* **65**, 1227–1233.

Ross S. D. (1974) Sulphates and other Oxy-anions of Group VI. In *The Infrared Spectra of Minerals* (ed. V. C. Farmer). Mineralogical Society of Great Britain and Ireland.

Rowsell J. and Nazar L. F. (2000) Speciation and thermal transformation in alumina sols: structures of the polyhydroxyoxoaluminum cluster $[Al_{30}O_8(OH)_{56}(H_2O)_{26}]^{18+}$ and its δ-Keggin Moieté. *J. Am. Chem. Soc.* **122**, 3777–3778.

Sánchez-España J., Pamo E. L., Pastor E. S., Andrés J. R. and Rubí J. A. M. (2006) The removal of dissolved metals by hydroxysulphate precipitates during oxidation and neutralization of acid mine waters, iberian pyrite belt. *Aquat. Geochem.* **12**, 269–298.

Sánchez-España J., Yusta I. and Diez-Ercilla M. (2011) Schwertmannite and hydrobasaluminite: a re-evaluation of their solubility and control on the iron and aluminium concentration in acidic pit lakes. *Appl. Geochem.* **26**, 1752–1774.

Sanjuan B., Millot R., Ásmundsson R., Brach M. and Giroud N. (2014) Use of two new Na/Li geothermometric relationships for geothermal fluids in volcanic environments. *Chem. Geol.* **389**, 60–81.

Schmid S. M., Fugenschuh B., Kissling E. and Schuste R. (2004) Tectonic map and overall architecture of the Alpine orogen. *Eclogae Geol. Helv.* **97**, 93–117.

Schönherr S. and Bertram R. (1983) IR-spektroskopische Charakterisierung basischer Aluminiumkationen. *Z. Chem.* **23**, 105 105.

Schönherr S., Görz H., Bertram R., Müller D. and Gessner W. (1983) Vergleichende Untersuchungen an unterschiedlich dargestellten basischen Aluminiumchloridlösungen. *Z. Anorg. Allg. Chem.* **502**, 112–122.

Schönherr S., Görz H. and Bertram R. (1987) Zur Anwendung der zeitabhängigen Komplexbildung mit Ferron für die Charakterisierung basische Metallkationen. *Wiss. Z. Päd. Hoschsch. Potsdam*, 31.

Singh S. S. and Brydon J. E. (1969) Solubility of basic aluminum sulfate at equilibrium insolution and in the presence of montmorillonite. *Soil Sci.* **107–1**, 12–16.

Swisstopo, 2017. Geographical Information Platform of the Swiss Confederation. Federal Office of Topography <https://map.geo.admin.ch> accessed on 1.9.2017.

Tien P. L. (1968) Hydrobasaluminite and basaluminite in Cabaniss formation (middle Pennsylvanian) southeastern Kansas. *Am. Mineral.* **53**, 722–732.

Totsche O., Pöthig R., Uhlmann W., Büttcher H. and Steinberg C. E. W. (2003) Buffering mechanisms in acidic mining lakes – a model-based analysis. *Aquat. Geochem.* **9**, 343–359.

Ulrich K. U. and Pöthig R. (2000) Precipitation of aluminium and phosphate affected by acidification. *Acta Hydroch. Hydrob.* **28**, 313–322.

Vaculikova L., Plevova E., Vallova S. and Koutnik I. (2011) Characterization and differentiation of kaolinites from selected Czech deposits using infrared spectroscopy and differential thermal analysis. *Acta Geodyn. Geomater.* **8**, 59.

Williamson M. A. and Rimstidt J. D. (1994) The kinetics and electrochemical rate-determining step of aqueous pyrite oxidation. *Geochim. Cosmochim. Acta* **58**, 5443–5454.

Associate editor: Jeffrey G. Catalano